Experimental and Theoretical Investigation of the Dynamics and Stability of Hanging Tubular Cantilevers Subject to Internal and External Flow

Sophie Lynn Minas

Master of Engineering

Department of Mechanical Engineering

McGill University

Montreal,Quebec

2017-08-15

A thesis submitted to McGill University in partial fulfillment of the requirements of the degree of Master of Engineering

DEDICATION

This document is dedicated to the graduate students of the McGill University.

ACKNOWLEDGEMENTS

First, I would like to thank my supervisor Michael Paidoussis for his continual guidance and support throughout my graduate studies. I am grateful to him for sharing his knowledge of fluid-structure interactions and for leading me in becoming a stronger researcher. Secondly, I would like to thank Professor Farhang Daneshmand for co-supervising my thesis and for challenging me. I am very grateful to my friends and colleagues: Matteo, Mohamad, Ahmed, Faisal, and Joachim for providing helpful feedback and for creating a positive laboratory environment. I would also like to thank my fellow Oozefest champions for showing me that any challenge can be met. I am ever grateful to my mother, father, and brother for advising me and helping me throughout my studies. Thank you also my dear Alan for being with me every step of the way. Finally, I would like to thank the Solution Mining Research Institute (SMRI) for funding this work, the Natural Sciences and Engineering Research Council (NSERC) of Canada, the Fluid-Structure Interactions Laboratory, and Mechanical Engineering Department at McGill University.

ABSTRACT

The fluid-elastic instability of hanging cantilevered tubes subject to internal and external flows has been studied. At high enough flow velocities, these flexible tubular cantilevers experience amplified oscillations (flutter) and/or static divergence (buckling). Specifically, the system studied consists of a flexible tubular hanging cantilever, which hangs concentrically within a larger diameter outer rigid tube. The fluid flows inside the cantilever as well as externally in the annular space. Two flow configurations are considered here. For configuration (iii)[1] , fluid is directed from the clamped end of the cantilever to the free end and flows in the opposite direction in the annular region between the cantilever and the outer tube. For the configuration (iv) case, the fluid is aspirated through the cantilever tube and discharged in the annular space. This entire system was contained within a closed cavity and immersed in surrounding fluid. Modification of the traditional system from axial to radial flow at the tube free end was accomplished with the use of end-pieces with holes perpendicular to the tube. The end-piece created an added mass effect in addition to diverting flow radially. For configuration (iv), experimental results indicated no changes in system behavior between axial and radial flow. For configuration (iii), the experimental results showed that discharging radial flow through the free end of the cantilever resulted in stability and no flutter, while cantilevers conveying axial flow

[1] Configurations (i) and (ii) have been previously studied and are not detailed in this thesis [17]

through the free end displayed loss of stability by flutter. A linear model is derived based on earlier work by Paidoussis et al. (2014), in which series solutions are employed using Euler-Bernoulli beam comparison functions and applying the Galerkin method, for configuration (iii) [23]. The experimental results are compared with the theoretical model results. The effects of end-piece mass, confinement, pipe length, and comparisons between radial and axial flow have also been studied. Theoretical predictions for this system were examined by varying several parameters including the mass of the end-piece (m_e), confinement length fraction (r_{ann}), and pipe length (L). The results indicated that, as the mass of the end-piece was increased, the cantilever was destabilized. With regards to confinement, experimentally stability was seen for all cases and theoretically predicted for most cases. Theoretically and experimentally, stability for all modes was seen for all tube lengths considered, suggesting that stability may be independent of cantilever length. This system is relevant to brine production as well as to the salt-cavern hydrocarbon storage industry, in which piping conveying brine/oil is subject to flow-induced vibrations and instabilities. Relevant brine-string system parameters were run in the theoretical model and resulted in stability for several combination of system parameters. Additionally, the ratio between external and internal flow velocity was investigated for configuration (iii) flow direction and proved that higher ratios have a de-stabilizing effect.

ABRÉGÉ

L'instabilité fluide-élastique des tubes suspendus en porte-à-faux et soumis à des écoulements internes et externes est étudiée. À des vitesses d'écoulement suffisamment élevées, ces tubes flexibles présentent oscillations dynamiques (battement) et/ou une divergence statique (flambage). Plus précisément, le système étudié se compose d'un encastré-libre, qui est suspendu de manière concentrique à l'intérieur d'un plus grand tube rigide externe. Le fluide circule à l'intérieur du porte-à-faux, ainsi à l'extérieur dans l'espace annulaire. Deux configurations d'écoulement sont considérées ici. Pour la configuration (iii),[2] le fluide est dirigé de l'extrémié serrée du porte-à-faux à l'extrémité libre et il écoule dans la direction opposée dans la région annulaire entre le porte-à-faux et le tube extérieur. Pour la configuration (iv), le fluide est aspiré dans le tube en porte-à-faux et déchargé dans l'espace annulaire. Ce système est entièrement contenu dans une cavité fermée et immergé dans un fluide. La modification de l'écoulement axial à un écoulement radial dans l'extrémité libre du tube a été réalisée en utilisant une extrémité avec de trous perpendiculaires à l'axe du tube. Cet embout crée un effet de masse ajouté en plus de dévier radialement l'écoulement. Pour la configuration (iv), les résultats expérimentaux n'ont pas montré un changement dans le comportement du système avec circulation axial ou radial. Pour la configuration (iii), les résultats expérimentaux ont montré que

[2] Les configurations (i) et (ii) ont déjà été étudiées détaillées dans cette thèse [17]

la décharge de l'écoulement radiale à l'extrémité libre du porte-à-faux a abouti à une stabilité et aucun flottement, tandis que les tubes avec un écoulement axial à l'extrémité libre ont montré une perte de stabilité avec du flottement. Un modèle linéaire a été dérivé sur la base de travaux antérieurs de Paidoussis et al. (2014), dans lesquels des solutions en série ont été employés en utilisant les fonctions propres des poutres Euler-Bernoulli et en appliquant la méthode de Galerkin pour la configuration (iii) [23]. Les résultats expérimentaux ont été comparés avec les résultats du modèle théorique. Les effets de la masse des extrémités, de l'enfouissement, de la longueur de la conduite et des comparaisons entre l'écoulement radial et axial ont également été étudiés. Les prédictions théoriques de ce système ont été examinées en variant plusieurs paramètres, tels que la masse de l'extrémité (m_e), le diamètre de l'anneau (r_{ann}) et la longueur du tube (L). Les résultats indiquent qu'avec un embout plus massif, le porte-à-faux était déstabilisé. En ce qui concerne le blocage partiel du tube, la stabilité expérimentale a été obtenue dans tous les cas et théoriquement prévue pour la plupart des cas. Théoriquement et expérimentalement, la stabilité de tous les modes a été observée pour toutes les longueurs de tube considérées, ce qui suggère que la stabilité peut être indépendante de la longueur en porte-à-faux. Ce système est pertinent pour la production de saumure ainsi que pour l'industrie du stockage des hydrocarbures à base de sel dans lequel la tuyauterie transmettant de la saumure / de l'huile est soumise à des vibrations et des instabilités induites par l'écoulement. Les paramètres du système de la saumure concernée ont été adoptés dans le modèle théorique et ont entraîné une stabilité pour plusieurs combinaisons de paramètres du système. En outre, le rapport entre la vitesse d'écoulement externe et

interne a été éudié pour la configuration (iii) et a montré que des ratios plus élevés ont un effet déstablissant.

TABLE OF CONTENTS

LIST OF TABLES

LIST OF FIGURES

CHAPTER 1
Introduction

1.1 Fluid structure interactions and applications

Fluid-structure interaction is the study of the interactions of an impressionable structure subject to an internal flow or surrounding fluid flow. Two main types of instability are considered here, buckling or static divergence as well as flutter or dynamic, amplified oscillations. An example of flow-induced buckling is the collapse of pliable shells. Physiologically for example, veins can collapse due to blood pressure, flow, and tissue interactions. Examples of flutter include the waving of flags in the wind or oscillatory motion of a free flowing garden hose. While flow-induced vibrations are typically considered to be a negative result of fluid-structure interactions, these vibrations are not always negative. Eels as well as other aquatic animals use these vibrations to move by self-propulsion. An additional example is how wind dynamics is responsible for seed dispersal for plants.

The fluid-structure interactions of pipes and cylinders conveying internal flow and/or subject to external flow are of particular academic and industrial interest. The case of a pipe conveying fluid has become a paradigm of dynamics given its usefulness in many engineering systems including nuclear reactors, heat exchangers, and countless others. The dynamical behavior of cantilevered pipes conveying fluid from the clamped end to the free end as well as reverse flow are of particular research interest.

Of present, fluid-elastic instability has been identified to cause bending and/or breaking of pipe-strings used in solution mining and hydrocarbon storage. As repair and replacement of the piping is expensive, investigation of such systems is desired. This thesis addresses the fluid-elastic instability of this system.

1.2 Background and motivation

1.2.1 SMRI Background

Solution mining is a process in which water-soluble minerals are extracted from drilled wells underground. Freshwater is pumped underground through very long tubes and dissolves the minerals including potash trona, magnesium and potassium salts forming a brine solution. The saturated brine solution is then extracted by pumping in fresh water. After, the minerals can be obtained from the saturated brine solution through a recryastallization process.

As a result of solution mining, underground caverns also called salt caverns are formed. These caverns are then used for underground storage of natural gas, crude oil, and other hydrocarbons and chemicals. In order to use these salt caverns for hydrocarbon storage, long pipes or pipe strings are lowered 1-2 km into the Earth's surface through a borehole. Brine-strings or very long hanging cantilever pipes are used to add/extract the hydrocarbon for example. The brine-string is clamped at the top of the cavern and is placed concentric with a larger diameter outer rigid pipe called the casing. The casing serves to support the borehole and does not extend the full length of the inner cantilevered pipe, leaving the inner pipe hanging freely near the bottom of the cavern. The product is added to the salt cavern by pumping the fluid through the pipe string. To extract the product, brine solution is injected

causing the product to be displaced and then flow through the annular space between the brine-string and the outer rigid pipe. These pipe strings are subject to bending and/or breaking as a result of suspected flow-induced vibrations at high enough flows and is the motivation for this thesis.

Several flow configurations are defined and named as configuration (i), (ii), (iii), and (iv). They are based on internal and external flow conditions that are relevant for salt cavern solution mining and hydrocarbon storage and they are described hereafter.

1. Configuration (i), the tube discharges fluid (flow from clamped end to free end) and there is no flow in the annulus
2. Configuration (ii), the tube aspirates fluid (flow from the free end to the clamped end) and there is no flow in the annulus
3. Configuration (iii), the tube discharges fluid and the annulus aspirates fluid
4. Configuration (iv), the tube aspirates fluid and the annulus discharges fluid

While all of these flow configurations are relevant to the application, configurations (i) and (ii) have been previously studied and addressed. Thus, configuration (iii) and (iv) are the primary focus of this thesis.

1.2.2 System studied

Several flow configurations relevant to different salt cavern solution mining and hydrocarbon storage are considered in this thesis including:

1. Configuration (iii) the tube discharging and the annulus aspirating fluid
2. Configuration (iv) the annulus discharging and the tube aspirating fluid

In the application, for configuration (iii) brine is added through the hanging pipe string, so that the hydrocarbon product is aspirated through the annular space. For configuration (iv), the reverse is true.

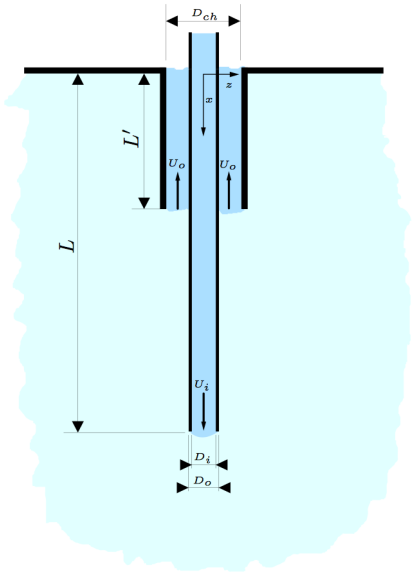

Figure 1–1: Schematic of the Drill-String System

1.3 Literature review

In this section, we build up to the concept of tubular cantilevers conveying fluid that are subject to external flow and immersed in fluid. Intuitively it is logical to break down this system following its historical development. Systems with internal flow and external flows are considered separately and then simultaneously. Thus, the literature review progresses as follows: discharging cantilevers, aspirating cantilevers, cantilevers subject to internal and external flows. For a more exhaustive review of the systems presented here, refer to [20], [22], and [23].

1.3.1 Discharging Cantilever

Previous work relating to this system includes studies addressing tubular cantilevers conveying fluid. An early study of the dynamics of cantilevers conveying fluid was completed by Benjamin, in which he considered an articulated cantilever pipe conveying fluid from a theoretical and experimental perspective [1]. An articulated cantilever system possesses N degrees of freedom and is a series of N rigid pipes which are interconnected by N flexible joints. From here, the continuous cantilever was considered for which N tends to infinity. By applying a Lagrangian approach to the system, Hamilton's principle for a system with infinite energy (due to continuous flow in and out of the system) was obtained for this system for a period of oscillations T. R denotes the position at the free end of the last pipe in the articulated system, τ is the unit vector in the tangential direction at the free end of the last pipe.
The expression

$$\Delta W = \int_0^T -MU(\dot{R}^2 + U\tau \cdot \dot{R})dt \tag{1.1}$$

denotes the work (ΔW) done on the pipe by the fluid forces.

Further, the linear equation of motion was derived as

$$EI\frac{\partial^4 w}{\partial x^4} + MU^2\frac{\partial^2 w}{\partial x^2} + 2MU\frac{\partial^2 w}{\partial x \partial t} + (M+m)\frac{\partial^2 w}{\partial t^2} = 0 \tag{1.2}$$

for the continuous pipe conveying fluid, where EI is flexural rigidity of the pipe, m is the mass of the tube per unit length, M is the mass of fluid, x is the longitudinal coordinate, w is the lateral coordinate, and U is the internal flow velocity. $MU^2\frac{\partial^2 w}{\partial x^2}$ is known as the centrifugal term, associated with the fluid forces in the curved portions of the pipe. $2MU\frac{\partial^2 w}{\partial x \partial t}$ is known as the Coriolis term. The last term corresponds

to the inertial force. Using this model, Benjamin predicted amplified oscillations or flutter for the articulated cantilever system for high enough internal flow.

This investigation was furthered by Gregory and Paidoussis, in which they considered a cantilever in a horizontal plane [7]. By applying a Newtonian approach to this system, they arrived at the same equation as Benjamin. To solve this equation, two methods were used. The first method was used to obtain exact solutions by setting $w(x,t) = Re[\sum_{j=1}^{4} A_j e^{i\Lambda_j x/L} \times e^{i\Omega_j t}]$ and applying cantilever boundary conditions. The second method of solution was an approximate method, solved by discretizing the system in terms of cantilever Euler-Beam eigenfunctions and using the Galerkin method. Amplified oscillations for this system were predicted for both the exact and approximate solutions. Experiments by Gregory and Paidoussis (1966) confirmed oscillatory behavior predicted theoretically [8]. Additionally, the effect of damping was also explored, and in some cases proved to be destabilizing.

In 1970, Paidoussis studied the dynamics of vertical hanging, cantilever pipes conveying internal flow, experimentally and theoretically [19]. In contrast with Benjamin, it was concluded that buckling does not occur for this system. For this system, flutter was the only type of instability observed experimentally. It was found that in the case of already buckled hanging cantilevers, internal flow actually served to re-stabilize the system, before flutter instability emerged after further increase in flow. Additionally, an expression for the work done on the cantilever by the fluid forces was developed over a period of oscillation, T, and is,

$$\Delta W = -MU \int_0^T \left((\frac{\partial w}{\partial t})^2 + U(\frac{\partial w}{\partial t})(\frac{\partial w}{\partial x}) \right) dt \tag{1.3}$$

This equation is consistent with the equation provided by Benjamin. For a simply supported pipe, i.e. a pipe with supported ends, $\frac{\partial w}{\partial t} = 0$ and as a result, $\Delta W = 0$. This is indicative of a gyroscopic conservative system. However, a cantilever pipe is a non-conservative system because $\Delta W \neq 0$. For small values of internal flow velocity, U, then $\Delta W < 0$ and motions of the pipe are damped, as energy flows from the pipe to the fluid. In the case of sufficiently large U, $\Delta W > 0$ and thus, the pipe gains energy from the fluid causing free motion of the pipe to become amplified. Physically, this corresponds to a dragging, lagging motion of the free end of the pipe, which was verified experimentally and was in line with previous work.

Paidoussis and Issid (1974) developed a linear equation of motion for a pipe conveying fluid [11]. In the following equation, gravity, damping based on the pipe material, dissipation to the surrounding fluid, effects of external tensioning and pressurization were considered. Additionally, variation in U was also accounted for.

$$\begin{aligned}(E^*\frac{\partial}{\partial t} + E)I\frac{\partial^4 w}{\partial x^4} + [MU^2 - \bar{T} + \bar{p}A(1-2\nu\delta)]\frac{\partial^2 w}{\partial x^2} \\ -[(M+m)g - M\frac{dU}{dt}](L-x)\frac{\partial^2 w}{\partial x^2} \\ +2MU\frac{\partial^2 w}{\partial x \partial t} + (M+m)g\frac{\partial w}{\partial x} + c\frac{\partial w}{\partial t} + (M+m)\frac{\partial^2 w}{\partial t^2} = 0\end{aligned} \tag{1.4}$$

E^* is the Kelvin-Voigt type dissipation of the pipe material, $\bar{T}$ is the external tension, $\bar{p}$ is the external pressurization, A is the internal cross-sectional area of the tube, ν is the Poisson ratio of the material of the pipe, δ is a binary parameter pertaining to axial sliding (equal to 0 when there is no contraint with respect to axial motion at $x = L$ and equal to 1 when axial motion is prevented for $x = L$),

M is the mass of the fluid per unit length, and m is the mass of the pipe per unit length.

In 2002, Doaré and Langre studied the flow induced instabilities of hanging fluid-conveying pipes [5]. Here, the effect of pipe length on the stability of this system was investigated. Experimentally and theoretically, it was determined that flutter in these systems becomes independent of pipe length, beyond a specific critical length. It was further explained that the stability of this hanging cantilever system is a balance between the internal flow and the force of gravity, while internal flow generates a de-stabilizing compressive force, the weight of the cantilever serves to stabilize the system due to an induced tension.

1.3.2 Aspirating Cantilever

The problem of the aspirating cantilever, with internal flow directed from the free end to the clamped end is a complex one. One of the earliest attempts made to understand this system was researched by Paidoussis (1998) [20]. An experimental investigation was completed by immersing a flexible pipe in a water reservoir with a pump used to drive flow from the free end to the clamped end. While stability was expected, the opposite occurred with the behavior characterized by amplified oscillations.

One application of the aspirating cantilever configuration, ocean mining, gave rise to further research into this problem. In ocean mining, a very long vacuum hose aboard a boat is extended to the ocean floor, where it sucks up mineral-rich sea-water. Modeling the behavior of this system, Paidoussis and Luu (1985) developed an analytical model for this system [24]. In this model, the internal flow velocity,

U was replaced with $-U$, simply to reverse the flow direction as compared to the discharging cantilever system and thus model the flow as a reverse jet. Theoretically, flutter for quite low flow velocities was predicted.

In 1999, Paidoussis modified the reverse jet assumption and instead modeled the flow into the free end of the cantilever as a sink flow [21]. Thus, flow entering the pipe free end undergoes a suction or a negative pressurization for which $\bar{p} = -\rho U^2 = \frac{-MU^2}{A}$. This pressurization effect was input into the following equation of motion

$$EI\frac{\partial^4 w}{\partial x^4} + (\bar{p}A + MU^2)\frac{\partial^2 w}{\partial x^2} + 2MU\frac{\partial^2 w}{\partial x \partial t} + (M+m)\frac{\partial^2 w}{\partial t^2} = 0 \tag{1.5}$$

and resulted in the cancellation of the centrifugal term, $(\bar{p}A + MU^2)\frac{\partial^2 w}{\partial x^2}$. Cancellation of this term implies that flutter cannot occur.

However, in 2005 Kuiper and Metrikine expressed the negative pressurization of the free end of the pipe as $\bar{p} = -\frac{1}{2}\rho U^2$, through the use of the Bernoulli equation. This result contradicted the expression for $\bar{p}$ suggested in 1999 [12]. Application of the newer expression meant that the centrifugal force did not completely cancel out and that flutter could emerge. Additionally, they also argued the aspirating pipe could still flutter as a result of the Coriolis term, even in the absence of the centrifugal term.

Around the same time, Kuiper and Metrikine (2008) as well as Giacobbi (2010) and Rinaldi (2009) showed that aspirating pipes lose stability through flutter for a defined critical flow velocity [13], [6], [25]. The motion of the pipe could be described as irregular motion consisting of first-mode orbital oscillations as well as quasi-chaotic

motions. ANSYS simulations completed by Giacobbi showed first mode flutter instability for a similar critical flow velocity. Adding to this investigation, Butt (2016) researched the aspirating cantilever system with water as the internal working fluid [3]. This system was also subject to counter-current external axial flow. The results of this experimentation showed a first mode flutter emerging for a specific critical flow velocity that then developed into second mode flutter with increasing internal flow.

1.3.3 Cantilevers subject to internal and external flows

In 1978, Hannoyer and Paidoussis researched the dynamics of confined cylindrical tubular beams subject to internal and external axial flows simultaneously [9]. This was completed for clamped-clamped and clamped-free boundary conditions. Attached to the end of the cantilevered tubes was a tapered end-piece. The equation of motion derived for this system was:

$$\begin{aligned} & E^*I\frac{\partial^5 w}{\partial x^4 \partial t} + EI\frac{\partial^4 w}{\partial x^4} + \rho_i A_i(\frac{\partial}{\partial t} + U_i\frac{\partial}{\partial x})^2 w \\ & + \rho_e A_e(\frac{\partial}{\partial t} + U_e^*\frac{\partial}{\partial x})(\frac{\partial}{\partial t} + U_e\frac{\partial}{\partial x}) - (\rho_e A_e - \rho_i A_i - m)g\frac{\partial w}{\partial x} \\ & - [T(L) - \int_x^L [(\rho_e A_e - \rho_i A_i - m)g - \frac{1}{2}C_{ft}\rho_e D_e U_e^2]dx]\frac{\partial^2 w}{\partial x^2} \\ & + \frac{1}{2}C_{fn}\rho_e D_e U_e(\frac{\partial}{\partial t} + U_e\frac{\partial}{\partial x}) + \frac{1}{2}\mu_e C_D\frac{\partial w}{\partial t} + m\frac{\partial^2 w}{\partial t^2} = 0 \end{aligned} \tag{1.6}$$

for which the sub-script i corresponds to internal and e corresponds to external, $T(L)$ as the tension at the free end. C_{ft}, C_{fn}, C_D are parameters accounting for viscous effects, please refer to [9] for details. The U_e^* is the flow velocity related to the development of the boundary layer. The associated boundary conditions for the two flow systems are given as:

$$\frac{\partial^2 w}{\partial x^2} = 0 \tag{1.7}$$

and

$$\begin{aligned}
&[(\rho + f\rho_e)\bar{A}_e + (\rho_i - \rho)A_i]l[\frac{\partial^2 w}{\partial t^2}]_L - f\rho_e(A_e - A_i)U_e^*[\frac{\partial w}{\partial t}]_L \\
&+ [f\rho_e(A_iU_e^* - \bar{A}_eU_e) + 2\rho_iA_iU_i]l[\frac{\partial^2 w}{\partial x \partial t}]_L - (E^*\frac{\partial}{\partial t} + E)I[\frac{\partial^3 w}{\partial x^3}]_L \\
&- [f\rho_e(A_e - A_i)U_eU_e^* + [(\rho_e - \rho)\bar{A}_e + (\rho - \rho_i)A_i]gl][\frac{\partial w}{\partial x}]_L = 0
\end{aligned} \tag{1.8}$$

for which $\bar{A}_e = \frac{1}{l}\int_L^{L+l} A_e(x)dx$, with $\bar{A}_e$ and f approximated as

$$\bar{A}_e \approx \frac{\frac{1}{3}(A_e^{\frac{3}{2}} - A_i^{\frac{3}{2}})}{(A_e^{\frac{1}{2}} - A_i^{\frac{1}{2}})} \tag{1.9}$$

$$f \approx \frac{4l^2}{4l^2 + (D_e - D_i)^2} \tag{1.10}$$

The length of the tapered end is l, A_e is the external area of the pipe, A_i is the internal pipe area, and $\bar{A}_e$ is an average area.

For a blunt end-piece for which $f \approx 0$, flutter instability was seen for sufficiently high internal flow velocity. The external flow velocity, U_e stabilized the system in this case. However, for a streamlined end-piece, both divergence and flutter were seen experimentally and theoretically.

In 2008, Paidoussis developed the equation of motion to model the dynamics of a drill-string system with floating, fluid powered drill-bit [15]. This system was modeled as hanging tubular cantilever with internal flow in the clamped-free direction and the external flow emerging from re-directing the internal flow axially upward

and counter-current to the internal flow. The equation of motion for this system was written as:

$$
\begin{aligned}
&EI\frac{\partial^4 w}{\partial x^4} + m\frac{\partial^2 w}{\partial t^2} + \rho_f A_f(\frac{\partial^2 w}{\partial t^2} + 2U_i\frac{\partial^2 w}{\partial x \partial t} + U_i^2\frac{\partial^2 w}{\partial x^2}) \\
&+ \chi\rho_f A_o(\frac{\partial^2 w}{\partial t^2} - 2U_o\frac{\partial^2 w}{\partial x \partial t} + U_o^2\frac{\partial^2 w}{\partial x^2}) - [(T - A_f\rho_i + A_o\rho_o)|_L \\
&+ (m + \rho_f A_f - \rho_f A_o)g(L-x) - \frac{1}{2}C_f\rho_f D_o U_o^2(1 + \frac{D_o}{D_h})(L-x)]\frac{\partial^2 w}{\partial x^2} \\
&+ [(m + \rho_f A_f - \rho_f A_o)g - \frac{1}{2}C_f\rho_f D_o U_o^2(1 + \frac{D_o}{D_h})]\frac{\partial w}{\partial x} \\
&+ \frac{1}{2}C_f\rho_f D_o U_o\frac{\partial w}{\partial t} + k\frac{\partial w}{\partial t} = 0
\end{aligned}
\tag{1.11}
$$

In this equation, ρ_f is the density of the fluid, D_i is the internal tube diameter, D_o is the external tube diameter for which A_f and A_o are calculated as the cross-sectional areas, respectively. The internal and external flow velocities are related through a simple continuity equation in which A_{ch} is the cross-sectional area of the annular region in which external flow aspirates

$$U_i A_i = U_o A_{ch} \tag{1.12}$$

For this system, it was found that U_o and U_i significantly impact the dynamics of the system. An additional parameter quantifying the confinement called $\alpha_{ch} = D_{ch}/D_o$, also impacted system behavior. It was found that for $\alpha_{ch} \geq 20$, the system was governed by internal flow and flutter instability was seen for sufficiently high internal flow velocity. This is logical, as a larger channel diameter corresponds to a

smaller U_o. For smaller values of α_{ch} however, smaller than 1.2, the external flow velocity caused de-stabilization of the system.

Further research into drill-string systems was characterized experimentally and theoretically by Moditis [17]. In this case, the cantilever was confined by a rigid outer tube that was shorter than the cantilever for partial confinement. Between the cantilever and the outer tube, annular, external flow aspirates. Experiments and theory confirmed the existence of flutter, with good agreement in terms of critical flow velocities. The theoretical model was extended to account for longer brine-string-like systems, and showed flutter as well as divergence instabilities depending on the specific system parameters.

1.4 End-Mass effect

The equation of motion developed by Gregory and Paidoussis [8], and earlier by Benjamin [1], was extended for a cantilevered pipe conveying fluid with an additional lumped mass. For this case, the original equation of motion is modified so that the $m\frac{\partial^2 w}{\partial t^2}$ term is replaced by

$$[m + \sum_{j=1}^{J} m_j \delta(x - x_j)] \frac{\partial^2 w}{\partial t^2} \tag{1.13}$$

with J lumped masses located at a distance x_j from the clamped end [10]. Results were obtained by the Galerkin method and the stability of the system was assessed as a function of β, defined as a ratio between the mass of the fluid divided by the mass of the fluid and the tube. Counter-intuitively, the effect of adding lumped

masses caused de-stabilization of the cantilever for most cases. This depended on the location of the lumped mass as well as the system parameters.

The three-dimensional vibrations of a hanging cantilever tube with a lumped mass at the free end was studied experimentally for a series of different end-mass weights [4]. Initial instability for this case was flutter, which then resulted in chaos.

An extension of the work undertaken by Copeland and Moon was completed by Paidoussis and Semler, with the motion constrained to be planar rather than three-dimensional motion [27]. Experimentally it was shown that even the presence of a small end-mass on the cantilever free end resulted in chaotic oscillations. The non-linear theoretical model predicted rich dynamical behavior consistent with the experimental results.

Additionally, Modarres-Sadeghi et al. further studied the dynamics of this system, reproducing analytically Copeland and Moon's experiments [16].

1.4.1 Discharging Radial flow

Hanging cantilevered pipes with an end-mass, discharging flow radially was considered by Rinaldi and Paidoussis [25], [26]. The external, surrounding fluid in this case was air. Experimentally, this resulted in stability of the cantilever, whereas usually flutter was seen for discharging axial flow. Additionally, a theoretical model was developed for this case, taking into account radial flow as well as the impact of an added-mass to the free end of the cantilever. For radial flow, the model previously developed by Hill and Swanson [10] was modified. For the case of radial flow, since straight-through flow is blocked the external tension term, $\bar{T}$ was set to be equivalent to MU^2. The result of this is the centrifugal term being eliminated from the

equation, leaving only the impact of the Coriolis force. As seen in equation (1.2) the Coriolis force introduces flow-induced damping preventing instability.

1.5 Research objectives

The system under consideration applies to salt cavern operations during solution mining and hydrocarbon storage processes. Specifically the system consists of a hanging tubular cantilever pipe that is subject to internal flow, external flow, and is immersed in a surrounding fluid. This flexible tube hangs concentrically within an outer rigid tube through which there is external flow and confinement effects. The aim of this research is to address this system in the following ways:

1. Experimentally and theoretically investigate flow-induced vibrations and instabilities of hanging brine-string systems that are used in solution mining and salt-cavern hydrocarbon storage industries
2. Understand specific flow configurations relevant to different modes of salt cavern operation. These flow configurations include configuration (iii) and (iv), in which for standard operating conditions flows are axial
3. Experimentally investigate the impact of radial flow on hanging brine-string system stability for configuration (iii) and (iv)
4. Compare configuration (iii) and (iv) behavior
5. Develop and apply a theoretical model for configuration (iii) with radial flow applying experimental and real life application brine-string parameters
6. Compare axial and radial flow behavior
7. Determine maximum flow velocities for which instability is avoided

8. Determine behavior and stability of partially confined cantilevered pipes conveying fluid in flow configuration (iii) for different ratios of external and internal flow velocities

CHAPTER 2
Theoretical Model

A linear theoretical model was derived for configuration (iii) with a radial flow end-piece on the cantilever free end. A schematic of the system is displayed in Figure (2–1a). The derivation of the system dynamics relates to work previously done in Moditis (2014) with modifications based on the added dynamics due to the addition of an end-piece with a non-negligible mass and radial flow [17].

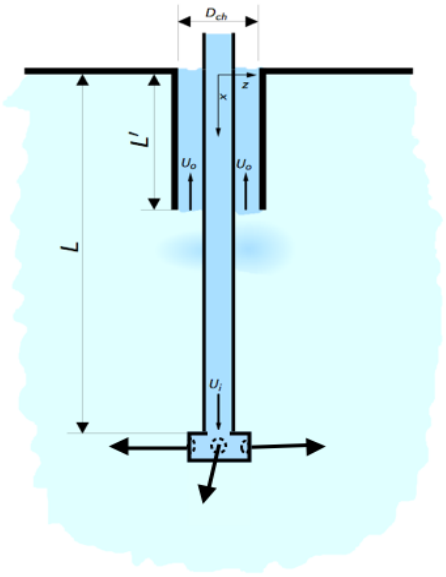

(a) Schematic of entire system

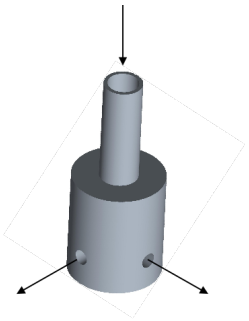

(b) Three-dimensional image of pipe end

Figure 2–1: Schematic of configuration (iii) system with radial flow

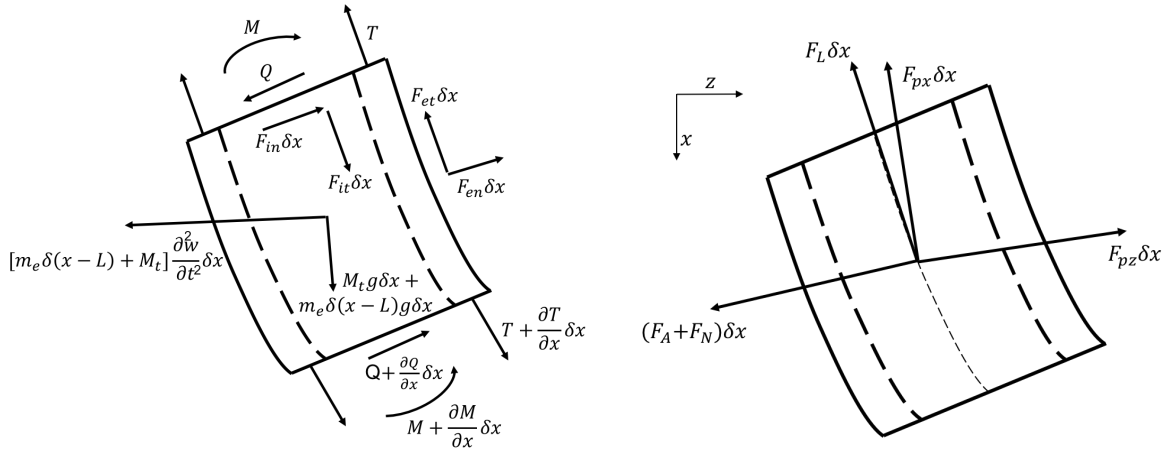

(a) Forces acting on an element of the tube of length δx

(b) Forces due to the outside fluid acting on the external surface of the tube element

Figure 2–2: Forces acting on a tube element

Structural and hydrodynamic forces are shown in Figure (2–2). A Newtonian approach was used to obtain the equations of motion based on these forces. The system studied consists of a uniform tubular cantilever beam of length L, external cross-sectional area A_o, mass per unit length M_t, mass of the end-piece m_e, and flexural rigidity EI. For a tubular element of length δx the structural and fluid-dynamic forces are added. Force balances in the x and z directions give equation. (2.1) and equation. (2.2), respectively

$$\frac{\partial T}{\partial x} - \frac{\partial}{\partial x}(Q\frac{\partial w}{\partial x}) + [M_t + m_e\delta(x-L)]g - (F_{in}+F_{en})\frac{\partial w}{\partial x} + F_{it} - F_{et} = 0 \qquad (2.1)$$

$$\frac{\partial}{\partial x}(T\frac{\partial w}{\partial x}) + \frac{\partial Q}{\partial x} - [M_t + m_e\delta(x-L)]\frac{\partial^2 w}{\partial t^2} + (F_{it}-F_{et})\frac{\partial w}{\partial x} + F_{in} + F_{en} = 0 \quad (2.2)$$

In equations (2.1) and (2.2), w is the lateral displacement, T is the tension in the tube, Q is the shear force, g the gravitation acceleration. The hydrodynamic forces due to internal flow include F_{in} in the normal direction and F_{it} in the tangential direction. The hydrodynamic forces due to external flow are given as F_{en} and F_{et} for the normal and tangential directions, respectively.

2.1 Structural Forces

Euler-Bernoulli beam theory is used to calculate the structural forces. This provides a logical approximation as the tube under consideration is slender and of uniform cross-section. Additionally we ignore viscoelastic damping effects and axial inertial effects. Thus, applying Euler-Bernoulli beam theory, the shear force is

$$Q = -\frac{\partial}{\partial x}(EI\frac{\partial^2 w}{\partial x^2}) \tag{2.3}$$

Substituting the equation for shear force into equations (2.1) and (2.2) and neglecting the higher order terms yields the following equations for the x and z directions:

$$\frac{\partial T}{\partial x} + [M_t + m_e\delta(x-L)]g + (F_{it} - F_{in}\frac{\partial w}{\partial x}) - F_{en}\frac{\partial w}{\partial x} - F_{et} = 0 \tag{2.4}$$

$$EI\frac{\partial^4 w}{\partial x^4} - \frac{\partial}{\partial x}(T\frac{\partial w}{\partial x} + (M_t + m_e\delta(x-L)))\frac{\partial^2 w}{\partial t^2} - (F_{in} + F_{it}\frac{\partial w}{\partial x}) - F_{en} + F_{et}\frac{\partial w}{\partial x} = 0 \tag{2.5}$$

2.2 Hydrodynamic Forces due to internal flow

The forces acting on an element of internal fluid of length δx are shown in Figure (2-2). The rate of change of momentum of the internal fluid is $M_f[\frac{\partial}{\partial t} + U_i\frac{\partial}{\partial x}]^2 w$ [22].

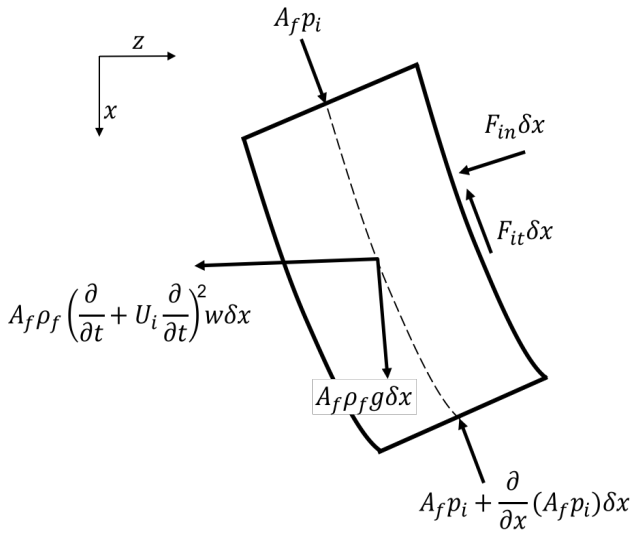

Figure 2–3: Forces Acting on an Element of Internally Flowing Fluid of Length δx

M_f is the mass of the internal fluid per unit length and is calculated as $M_f = \rho_f A_f$, where p_i is the internal pressure in the pipe, ρ_f is the density of the fluid and A_f is the cross-sectional area of the internal flow. Balancing the forces and applying the momentum equation, gives the following equations in the $x-$ and $z-$ directions:

$$F_{it} - F_{in}\frac{\partial w}{\partial x} = M_f g - \frac{\partial}{\partial x}(A_f p_i) \tag{2.6}$$

and

$$-(F_{in} + F_{it}\frac{\partial w}{\partial x}) = M_f(\frac{\partial}{\partial t} + U_i\frac{\partial}{\partial x})^2 w + \frac{\partial}{\partial x}(A_f p_i\frac{\partial w}{\partial x}) \tag{2.7}$$

By substituting equations (2.4) and (2.5) into equations (2.1) and (2.2), the effects of internal flow are summarized in the following equations:

$x-$ direction:

$$\frac{\partial T}{\partial x} + [M_t + m_e\delta(x-L)]g + [M_f g - \frac{\partial}{\partial x}(A_f p_i)] - F_{en}\frac{\partial w}{\partial x} - F_{et} = 0 \tag{2.8}$$

$z-$ direction:

$$\begin{aligned} &EI\frac{\partial^4 w}{\partial x^4} - \frac{\partial}{\partial x}(T\frac{\partial w}{\partial x}) + [M_t + m_e\delta(x-L)]\frac{\partial^2 w}{\partial t^2} - [M_f(\frac{\partial}{\partial t} + U_i\frac{\partial}{\partial x})^2 w \\ &+ \frac{\partial}{\partial x}(A_f p_i)\frac{\partial w}{\partial x}] - F_{en} + F_{et}\frac{\partial w}{\partial x} = 0 \end{aligned} \tag{2.9}$$

2.3 Hydrodynamic Forces due to External Flow

A sum of the external hydrodynamic forces acting on the tube (Figure (2–2)) gives resultant forces F_{en} and F_{et}. These forces due to external flow are comprised of several forces including, F_A, the lateral inviscid hydrodynamic forces, F_{px} and F_{pz}, the forces due to the outside mean pressure, F_N and F_L, the frictional viscous forces. A balance of these forces due to external flow are:

in the x- direction:

$$-F_{en}\frac{\partial w}{\partial x} - F_{et} = -F_L - F_{px} \tag{2.10}$$

in the z- direction:

$$-F_{en} + F_{et}\frac{\partial w}{\partial x} = F_A + F_N - F_{pz} + F_L\frac{\partial w}{\partial x} \tag{2.11}$$

For the development of the lateral inviscid hydrodynamic force, the external flow surrounding the tube is considered to be a potential flow [14], [22]. Additionally, slender-body theory is applied to the flow, under the assumption that $d << L$ (where

d is tube diameter and L is tube length) and that lateral variations are small. As proposed by Lighthill (1960), the inviscid hydrodynamic force per unit length is equal and opposite to the rate of change of the fluid momentum and can be written as $[(\frac{\partial}{\partial t}) - U_o(\frac{\partial}{\partial x})](M_f v_f)$ in which U_o is the external flow velocity, M_f is the added mass of the fluid per unit length, and v_f is the relative fluid velocity. The expression for the added mass for an unconfined tube is the following [22]:

$$M_a = \chi \rho_f Ao \tag{2.12}$$

$$A_o = \frac{\pi Do^2}{4} \tag{2.13}$$

in which the parameter A_o is the outer cross-sectional area based on the outer diameter of the tube (D_o). This equation for added mass is modified to account for the spatial variation as the annulus only covers a fraction of the full length of the tube [14], [22]. Thus, a Heaviside step function (H) and a confinement parameter (χ) are implemented to account for the variation in confinement along the length of the tube [17],

$$M_a = [\chi + (1 - \chi)H(x - L')]\rho_f A_o \tag{2.14}$$

$$\chi = \frac{\left(\frac{D_{ch}}{Do}\right)^2 + 1}{\left(\frac{D_{ch}}{Do}\right)^2 - 1} j \tag{2.15}$$

The Heaviside step function and χ are used in combination to account for the variation in external flow velocity, which is assumed to be zero over the unconfined portion of the tube, and U_o over the confined portion of the cantilever. An additional parameter, D_{ch} represents the channel diameter as seen in Figure (2–1a). Hence, accounting for the spatial variation of the fluid added mass as well as the variation in external flow velocity, the lateral inviscid hydrodynamic force or lift force is given as [18],

$$\begin{aligned} F_A = &(\frac{\partial}{\partial t} - U_o\frac{\partial}{\partial x} + U_o H(x-L')\frac{\partial}{\partial x})\times \\ &\{[\chi + (1-\chi)H(x-L')]\rho_f A_o(\frac{\partial w}{\partial t} - U_o\frac{\partial w}{\partial x} + U_o H(x-L')\frac{\partial w}{\partial x})\} \end{aligned} \tag{2.16}$$

and can be simplified to,

$$\begin{aligned} F_A = &-A_o U_o^2 \rho_f \chi H(x-L')\frac{\partial^2 w}{\partial x^2} + A_o U_o^2 \rho_f \chi \frac{\partial^2 w}{\partial x^2} + 2A_o U_o \chi H(x-L')\frac{\partial^2 w}{\partial x^2} \\ &- 2A_o U_o \rho_f \chi \frac{\partial^2 w}{\partial x \partial t} + (1-\chi)\rho_f A_o H(x-L')\frac{\partial^2 w}{\partial t^2} + A_o \rho_f \chi \frac{\partial^2 w}{\partial t^2} \end{aligned} \tag{2.17}$$

The frictional force due to the external flow velocity in the longitudinal direction is expressed as [17]

$$F_L = \frac{1}{2} C_f \rho_f D_o U_o^2 [1 - H(x-L')] \tag{2.18}$$

The coefficient of friction (C_f) is given a value of 0.0125, in accordance with previously documented work.

The frictional force in the normal direction is

$$F_N = \frac{1}{2} C_f \rho_f D_o U_o [1 - H(x - L')] \{ \frac{\partial w}{\partial t} - [1 - H(x - L')] U_o \frac{\partial w}{\partial x} \} + k \frac{\partial w}{\partial x} \quad (2.19)$$

Again, Heaviside step functions are used to account for the variation in external flow velocity along the length of the tube. The parameter k is the viscous drag coefficient, and is dependent on the oscillation frequency of the tube,

$$k = \frac{2\sqrt{2}}{\sqrt{S}} \frac{1 + \bar{\gamma}^3}{(1 - \bar{\gamma}^2)^2} \rho_f A_o R(\Omega) \quad (2.20)$$

The Stokes number, S, kinematic viscosity of the fluid ν, and $\bar{\gamma}$ (another measure of confinement based on diameter of the tube with respect to diameter of the outer annular region) are additional parameters in this equation:

$$S = \frac{R(\Omega) D_o^2}{4\nu} \quad (2.21)$$

$$\bar{\gamma} = \frac{D_o}{D_{ch}} \quad (2.22)$$

Since the parameter k also varies along the length of the tube, an additional parameter k_u is defined as [28]

$$k_u = \frac{2\sqrt{2}}{\sqrt{S}} \rho_f A_o R(\Omega) \quad (2.23)$$

resulting in the following simplified equation for the normal frictional force

$$F_N = \frac{1}{2}C_f\rho_f D_o U_o[1-H(x-L')]\{\frac{\partial w}{\partial t} - [1-H(x-L')]U_o\frac{\partial w}{\partial x}\} + k_u[\frac{1+\bar{\gamma}^3}{(1-\bar{\gamma}^2)^2} + H(x-L')(1-\frac{1+\bar{\gamma}^3}{(1-\bar{\gamma}^2)^2})]\frac{\partial w}{\partial t} \tag{2.24}$$

The mean external pressure acting on the cantilever in the x and z directions are defined below, respectively [22]:

$$F_{px} = -\frac{\partial}{\partial x}(A_o p_o) + A_o\frac{\partial p_o}{\partial x} \tag{2.25}$$

$$F_{pz} = A_o\frac{\partial}{\partial x}(p_o\frac{\partial w}{\partial x}) \tag{2.26}$$

in which p_o is the pressure outside the tube.

A force balance of the flow in the annular space yields

$$-A_{ch}\frac{\partial p_o}{\partial x} + F_f + A_{ch}\rho_f g = 0 \tag{2.27}$$

where $A_{ch} = \pi(D_{ch}^2 - D_o^2)$ is the area of the annular region and $F_f = F_L\frac{S_{tot}}{S_o}$ is the total frictional force. The total wetted area of annular flow per unit length is defined as S_{tot} and S_o is the external wetted perimeter of the tube.

$$S_{tot} = \pi(D_{ch} + D_o) \tag{2.28}$$

Substituting F_f into equation (2.28), multiplying through by $(\frac{A_o}{A_{ch}})$, and simplifying gives

$$A_o\frac{\partial p_o}{\partial x} = F_L\frac{D_o}{D_h} + A_o\rho_f g \tag{2.29}$$

The parameter D_h is the hydraulic diameter of the annular channel and is expressed as $D_h = \frac{4A_o}{S_{tot}} = (D_{ch} - D_o)$ An expression for the external pressure, p_o is defined by integrating equation (2.29) from 0 to L'. The value of the external pressure at $x = 0$ is equal to zero

$$p_o(x) = [\frac{F_L}{A_o}\left(\frac{D_o}{D_h}\right) + \rho_f g]x \tag{2.30}$$

For the portion of the cantilever between lengths L' and L or the unconfined portion, the external pressure distribution is assumed to be hydrostatic and is represented by the following equation

$$\frac{\partial p_o}{\partial x} = \rho_f g; \tag{2.31}$$

integrating yields,

$$p_o = \rho_f g x + C_1 \tag{2.32}$$

Relating the pressures at a location x_1 (an axial location just inside the annulus) and x_2 (an axial location just outside the annulus) yields

$$p_o|_{x_2} = p_o|_{x_1} + \frac{1}{2}\rho_f U_o^2 + \rho_f g h_a \tag{2.33}$$

where $h_a = K_1 \frac{U_o^2}{2g}$ is the head-loss due to stagnant fluid entering the annulus and K_1 is an estimate for the pressure loss due to fluid acceleration and is between 0.8 and 0.9 [2]. Therefore,

$$C_1 = \rho_f g x + [\frac{\frac{1}{2}C_f \rho_f D_o U_o^2}{A_o}\left(\frac{D_o}{D_h}\right) L'] + \frac{1}{2}\rho_f U_o^2 + \rho_f g h_a \tag{2.34}$$

Combining equations (2.30), (2.32), and (2.33) gives the pressure distribution over the entire cantilever length

$$\begin{aligned} p_o = & \frac{\frac{1}{2}C_f\rho_f D_o U_o^2}{A_o}\left(\frac{D_o}{D_h}\right)x - \frac{\frac{1}{2}C_f\rho_f D_o U_o^2}{A_o}\left(\frac{D_o}{D_h}\right)(x-L')H(x-L') + \rho_f g x \\ & + [\frac{1}{2}\rho_f U_o^2 + \rho_f g h_a]H(x-L') \end{aligned} \tag{2.35}$$

and the pressure gradient as

$$\frac{\partial p_o}{\partial x} = \frac{\frac{1}{2}C_f\rho_f D_o U_o^2}{A_o}\left(\frac{D_o}{D_h}\right)[1-H(x-L')] + \rho_f g + [\frac{1}{2}\rho_f U_o^2 + \rho_f g h_a]\delta_D(x-L') \tag{2.36}$$

where δ_D is the Dirac delta function.

Equations (2.18)and (2.25) are substituted into equation (2.10) and further substitution into equation (2.8) yields

$$\begin{aligned} & \frac{\partial}{\partial x}(T - A_f p_i + A_o p_o) + [M_t + m_e\delta(x-L)]g + M_f g - A_o\frac{\partial p_o}{\partial x} \\ & - \frac{1}{2}C_f\rho_f D_o U_o^2[1-H(x-L')] = 0 \end{aligned} \tag{2.37}$$

as the equation of motion in the x direction.

To obtain the balance of forces on the cantilever in the z direction equations (2.24),(2.18), (2.17), and (2.26) are substituted into (2.11) and further substitution

into (2.9) gives

$$
\begin{aligned}
&EI\frac{\partial^4 w}{\partial x^4} - \frac{\partial}{\partial x}[(T - A_f p_i + A_o p_o)\frac{\partial w}{\partial x}] + [M_t + m_e\delta(x-L)]\frac{\partial^2 w}{\partial t^2} + A_f\rho_f\frac{\partial^2 w}{\partial t^2} \\
&+ 2U_i A_f\rho_f\frac{\partial^2 w}{\partial x\partial t} + A_f\rho_f U_i^2\frac{\partial^2 w}{\partial x^2} - A_o U_o^2\rho_f\chi H(x-L')\frac{\partial^2 w}{\partial x^2} + A_o U_o^2\rho_f\chi\frac{\partial^2 w}{\partial x^2} \\
&+ 2A_o U_o\rho_f\chi H(x-L')\frac{\partial^2 w}{\partial x\partial t} - 2A_o U_o\rho_f\chi\frac{\partial^2 w}{\partial x\partial t} + (1-\chi)\rho_f A_o H(x-L')\frac{\partial^2 w}{\partial t^2} \\
&+ A_o\rho_f\chi\frac{\partial^2 w}{\partial t^2} + \frac{1}{2}C_f\rho_f D_o U_o[1 - H(x-L')]\frac{\partial w}{\partial t} \\
&+ k_u[\frac{1+\bar{\gamma}^3}{(1-\bar{\gamma}^2)^2} + H(x-L')(1 - \frac{1+\bar{\gamma}^3}{(1-\bar{\gamma}^2)^2})]\frac{\partial w}{\partial t} = 0
\end{aligned}
\tag{2.38}
$$

An expression for the tensioning and pressurization term is given below

$$
\begin{aligned}
&T - A_f p_i + A_o p_o = \\
&- (-M_t - m_e\delta(x-L') - \rho_f A_f + \rho_f A_o)g(L-x) \\
&- \frac{1}{2}C_f\rho_f D_o U_o^2\left(\frac{D_o}{D_h} + 1\right)(L'-x)[1 - H(x-L')] \\
&- A_o(\frac{1}{2}\rho_f U_o^2 + \rho_f g h_a)[1 - H(x-L')] + (T - A_f p_i + A_o p_o)|_L
\end{aligned}
\tag{2.39}
$$

and is found through the integration of equation (2.37) from x to L.

Substituting the expression for tensioning and pressurization into equation (2.38) yields

$$
\begin{aligned}
&EI\frac{\partial^4 w}{\partial x^4} + \{[M_t + m_e\delta(x-L) + \rho_f A_f - \rho_f A_o]g \\
&- \frac{1}{2}C_f\rho_f D_o U_o^2\left(\frac{D_o}{D_h}+1\right)[1-H(x-L')] - A_o[\frac{1}{2}\rho_f U_o^2 + \rho_f g h_a]\delta_D(x-L')\}\frac{\partial w}{\partial x} \\
&+ \{(-M_t - m_e\delta(x-L) - \rho_f A_f + \rho_f A_o)g(L-x) \\
&+ \frac{1}{2}C_f\rho_f D_o U_o^2\left(\frac{D_o}{D_h}+1\right)(L'-x)[1-H(x-L')] \\
&+ A_o[\frac{1}{2}\rho_f U_o^2 + \rho_f g h_a][1-H(x-L')] - (T - A_f p_i + A_o p_o)|_L\}\frac{\partial^2 w}{\partial x^2} \\
&+ [M_t + m_e\delta(x-L)]\frac{\partial^2 w}{\partial t^2} + A_f\rho_f\frac{\partial^2 w}{\partial t^2} + 2U_i A_f\rho_f\frac{\partial^2 w}{\partial x\partial t} \\
&+ A_f\rho_f U_i^2\frac{\partial^2 w}{\partial x^2} + A_o\rho_f\chi U_o^2[1-H(x-L')]\frac{\partial^2 w}{\partial x^2} - 2A_o U_o\rho_f\chi[1-H(x-L')]\frac{\partial^2 w}{\partial x\partial t} \\
&+ (1-\chi)\rho_f A_o H(x-L')\frac{\partial^2 w}{\partial t^2} + A_o\rho_f\chi\frac{\partial^2 w}{\partial t^2} + \frac{1}{2}C_f\rho_f D_o U_o[1-H(x-L')]\frac{\partial w}{\partial t} \\
&+ k_u\{[1 + [1-H(x-L')]\left(\frac{1+\bar{\gamma}^3}{(1-\bar{\gamma}^2)^2}-1\right)\}\frac{\partial w}{\partial t} = 0
\end{aligned}
\tag{2.40}
$$

with the standard cantilever boundary conditions

$$
w|_{x=0} = \frac{\partial w}{\partial x}|_{x=0} = \frac{\partial^2 w}{\partial x^2}|_{x=L} = \frac{\partial^3 w}{\partial x^3}|_{x=L} = 0 \tag{2.41}
$$

The internal and external/outside pressures can be related through the following relationship

$$
p_i|_L = p_o|_L - \frac{\rho_f U_i^2}{2} + \rho_f g h_e \tag{2.42}
$$

where h_e is the head-loss parameter [2], with $K_2 = 1$

$$
h_e = \frac{K_2 U_i^2}{2g} \tag{2.43}
$$

The external pressure can be calculated by evaluating equation (2.38) at $x = L$.

$$p_o|_L = \frac{1}{2A_o} C_f \rho_f D_o U_o^2 L' \left(\frac{D_o}{D_h}\right) + \rho_f g L + \frac{1}{2}\rho_f U_o^2 + \rho_f g h_a \tag{2.44}$$

Through a simple conservation of mass, the internal and external flow velocities are related,

$$U_o = U_i \frac{D_i^2}{D_{ch}^2 - D_o^2} \tag{2.45}$$

To account for radial flow at the free end of the pipe, the tension force is adjusted. Since flow is entirely radial and straight-through flow is blocked, a tensile force is generated, resulting in $T = M_f U_i^2$.

2.4 Non-dimensionalization

The governing equation of motion is non-dimensionalized through the use of the following parameters [17], [22]:

$$\begin{aligned}
&\xi = \frac{x}{L} \qquad \eta = \frac{w}{L} \qquad \tau = [\frac{EI}{M_t + \rho_f A_f + \rho_f A_o}]^{\frac{1}{2}} \frac{t}{L^2} \qquad \Gamma_e = \frac{m_e}{(M_t + \rho_f A_f - \rho_f A_o)L} \\
&u_i = \left(\frac{\rho_f A_f}{EI}\right)^{\frac{1}{2}} L U_i \qquad u_o = \left(\frac{\rho_f A_o}{EI}\right)^{\frac{1}{2}} L U_o \qquad \beta_o = \frac{\rho_f A_o}{M_t + \rho_f A_f + \rho_f A_o} \\
&\beta_i = \frac{\rho_f A_f}{M_t + \rho_f A_f + \rho_f A_o} \qquad \gamma = \frac{(M_t + \rho_f A_f - \rho_f A_o) g L^3}{EI} \qquad \Gamma = \frac{T|_L L^2}{EI} \\
&\Pi_{iL} = \frac{p_i|_L A_f L^2}{EI} \qquad \Pi_{oL} = \frac{p_o|_L A_o L^2}{EI} \qquad c_f = \frac{4C_f}{\pi} \\
&\kappa_u = \frac{k_u L^2}{[EI(M_t + \rho_f A_f + \rho_f A_o)]^{\frac{1}{2}}} \qquad \epsilon = \frac{L}{D_o} \qquad h = \frac{D_o}{D_h} \\
&\alpha = \frac{D_i}{D_o} \qquad \alpha_{ch} = \frac{D_{ch}}{D_o} \qquad r_{ann} = \frac{L'}{L}
\end{aligned} \tag{2.46}$$

The resulting non-dimensional form of equation of motion (2.40) is

$$\begin{aligned}
&\frac{\partial^4\eta}{\partial\xi^4} + [\gamma - \frac{1}{2}c_f u_o^2(1+h)[1-H(\xi-r_{ann})]\frac{\partial\eta}{\partial\xi} \\
&- \frac{1}{2}u_o^2(1+K_1)\delta_D(\xi - r_{ann} + \gamma\Gamma_e\delta(\xi-1))\frac{\partial\eta}{\partial\xi} \\
&- \{(\Gamma - \Pi_{iL} + \Pi_{oL}) + \gamma(1-\xi) - \frac{1}{2}c_f\epsilon u_o^2(1+h)(r_{ann}-\xi)[1-H(\xi-r_{ann})] \\
&- \frac{1}{2}u_o^2(1+K_1)[1-H(\xi-r_{ann})] - \gamma\Gamma_e\delta(\xi-1) + \gamma\Gamma_e\xi\delta(\xi-1)\}\frac{\partial^2\eta}{\partial\xi^2} \\
&\{1 + \beta_o(\chi-1)[1-H(\xi-r_{ann})] + \Gamma_e\delta(\xi-1)\}\frac{\partial^2\eta}{\partial\tau^2} \\
&+ 2\{u_i\beta_i^{\frac{1}{2}} - \chi u_o\beta_o^{\frac{1}{2}}[1-H(\xi-r_{ann})]\}\frac{\partial^2\eta}{\partial\xi\partial\tau} + \\
&\{u_i^2 + \chi u_o^2[1-H(\xi-r_{ann})]\}\frac{\partial^2\eta}{\partial\xi^2} + \frac{1}{2}c_f\epsilon u_o\beta_o^{\frac{1}{2}}[1-H(\xi-r_{ann})]\frac{\partial\eta}{\partial\tau} \\
&+ \kappa_u\{[1 + [1-H(\xi-r_{ann})]\left(\frac{1+\alpha_{ch}^{-3}}{(1-\alpha_{ch}^{-2})^2} - 1\right)\}\frac{\partial\eta}{\partial\tau} = 0
\end{aligned} \tag{2.47}$$

with the non-dimensional boundary conditions

$$\eta|_{\xi=0} = \frac{\partial\eta}{\partial\xi}|_{\xi=0} = \frac{\partial^2\eta}{\partial\xi^2}|_{\xi=1} = \frac{\partial^3\eta}{\partial\xi^3}|_{\xi=1} = 0 \tag{2.48}$$

Additionally, the dimensional frequency Ω is translated to the non-dimensional frequency ω through the following relationship

$$\omega = [\frac{M_t + \rho_f A_f + \rho_f A_o}{EI}]^{\frac{1}{2}}L^2\Omega \tag{2.49}$$

The internal pressure equation is non-dimensionalized to

$$\Pi_{iL} = \alpha^2\Pi_{oL} - \frac{1}{2}u_i^2 + A_f\rho_f g h_e(\frac{L^2}{EI}) \tag{2.50}$$

and the external pressure equation is non-dimensionalized to

$$\Pi_{oL} = \frac{1}{2} c_f h r_{ann} \epsilon u_o^2 + \frac{1}{2} u_o^2 (1 + K_1) + \frac{A_o \rho_f g L^3}{EI} \tag{2.51}$$

The non-dimensional flow velocity relationship is

$$u_o = \frac{\alpha}{\alpha_{ch}^2 - 1} u_i \tag{2.52}$$

'The non-dimensionalized tension generated by the blocking of straight-through flow and diverting flow radially is given as $\Gamma = u_i^2$.

2.5 Method of Solution

The Galerkin method [22] is applied to the governing equation of motion (2.47), assuming an approximate solution of

$$\eta(\xi, \tau) = \sum_{j=1}^{N} \Phi_j(\xi) q_j(\tau) \tag{2.53}$$

$\Phi_j(\xi)$ are Euler-Bernoulli beam cantilever beam eigenfunctions used as comparison functions and $q_j(\tau)$ are the generalized coordinates of the system with $q_j(\tau) = e^{i\omega_j \tau}$.

The following integral relations are defined with the bounds of integration for $(0, 1)$ for the entire length of the tube and for $(0, r_{ann})$ representing the confined portion of the tube

$$\begin{aligned} a_{ij(a,b)} &= \int_a^b \Phi_i \Phi_j d\xi \qquad & b_{ij(a,b)} &= \int_a^b \Phi_i \frac{d\Phi_j}{d\xi} d\xi \\ c_{ij(a,b)} &= \int_a^b \Phi_i \frac{d^2\Phi_j}{d\xi^2} d\xi \qquad & d_{ij(a,b)} &= \int_a^b \xi \Phi_i \frac{d^2\Phi_j}{d\xi^2} d\xi \end{aligned} \tag{2.54}$$

Equations (2.53) and (2.54) are substituted into equation (2.40), pre-multipliplied by Φ_i and integrated from $\xi = 0$ to $\xi = 1$. Finally, the equation of motion is written

in the form, $M\ddot{q}+C\dot{q}+Kq=0$ where $\dot{()}$ denotes a derivative with respect to τ, and

$$
\begin{aligned}
M_{ij} &= a_{ij(0,1)} - \beta_o(1-\xi)a_{ij(0,r_{ann})} + \Gamma_e\Phi_i(1)\Phi_j(1) \\
C_{ij} &= 2u_i\beta_i^{\frac{1}{2}}b_{ij(0,1)} - 2\chi uo\beta_o^{\frac{1}{2}}b_{ij(0,r_{ann})} + \frac{1}{2}c_f\epsilon u_o\beta_o^{\frac{1}{2}}a_{ij(0,r_{ann})} + \kappa_u a_{ij(0,1)} \\
&\quad + \kappa_u\left(\frac{1+\alpha_{ch}^{-3}}{(1-\alpha_{ch}^{-2})^2}-1\right)a_{ij(0,r_{ann})} \\
K_{ij} &= \lambda_j^4 a_{ij(0,1)} + \gamma b_{ij(0,1)} - \frac{1}{2}c_f\epsilon u_o^2(1+h)b_{ij(0,r_{ann})} \\
&\quad - \frac{1}{2}u_o^2(1+K_1)(\Phi_i|_{\xi=r_{ann}}\frac{\partial\Phi_j}{\partial\xi}|_{\xi=r_{ann}}) - (\Gamma-\Pi_{iL}+\Pi_{oL})c_{ij(0,1)} \\
&\quad - \gamma(c_{ij(0,1)}-d_{ij(0,1)}) + \frac{1}{2}c_f\epsilon u_o^2(1+h)(r_{ann}(c_{ij(0,r_{ann})}-d_{ij(0,r_{ann})})) \\
&\quad + \frac{1}{2}u_o^2(1+K_1)c_{ij(0,1)} + u_i^2c_{ij(0,1)} + \chi u_o^2c_{ij(0,r_{ann})} \\
&\quad \gamma\Gamma_e\Phi_i(1)\frac{\partial\Phi_j}{\partial\xi}(1) - \gamma\Gamma_e c_{ij(0,1)}
\end{aligned}
\tag{2.55}
$$

CHAPTER 3
Theoretical Model Results

3.1 Theoretical Results for Experimental Parameters

Dimensional and non-dimensional parameters consistent with Table 3-1 were input into this theoretical model. These values are consistent with the experimental parameters. The * parameters in the table indicate parameters that were varied experimentally.

Table 3–1: Dimensional and Non-Dimensional Parameters used Experimentally and Applied Theoretically

D_i [m]	D_o [m]	D_{ch} [m]	L *[m]
0.00635	0.016	0.0315	0.456
$L'*$ [m]	EI $[Nm^2]$	M_t $[kgm^{-1}]$	m_e [kg]
0.214	0.00737	0.194	0.008
α	α_{ch}	ϵ	β_i
0.397	1.97	28.5	0.0742
β_o	h	γ	r_{ann}*
0.471	1.03	3.14	0.453

Theoretical results for the parameters given in Table 3-1 are presented in Argand diagrams plotting the real and imaginary components of the eigenfrequencies.

Instability/stability of the modes was then assessed. Instability occurs when the imaginary component of the eigenfreqeuncy becomes negative; if the corresponding real eigenfrequency is zero and the critical frequency is zero, this indicates a buckling instability. However, if the corresponding real eigenfrequency is non-zero, this is a flutter instability. Thus, if both eigenfrequency components remain positive, the mode is stable. In the Argand diagrams, the data labels correspond to each internal flow velocity point; the internal flow velocity U_i was increased from 0 to 12 m/s. A minimum of 11 modes were used to satisfy convergence criteria. Results for the first two modes are of primary focus for stability assessment, as these are the modes that are known to be excited experimentally and/or in the drill-string application.

3.1.1 Effect of Confined Length Fraction r_{ann}

The confined length fraction (r_{ann}) is a ratio between the length of the annulus and the total length of the cantilever (L'/L). This parameter was varied experimentally for r_{ann}=0, 0.239, 0.453, and 0.668 by changing the length of the rigid outer tube (L') and keeping the cantilever length (L) constant (Figure (3-1)). For an unconfined tube or for r_{ann}=0, the first four modes are stable for the entire flow velocity range. For the exact parameters given in Table 1 with r_{ann}=0.453, the first mode is stabl,e while the second mode loses stability by flutter for a critical flow velocity of 5.1 m/s and a critical frequency of 22.7 rad/s, as this is where the imaginary ω becomes less than zero. For the other confined tubes, in which r_{ann}=0.239 and 0.668, the first two modes are stable.

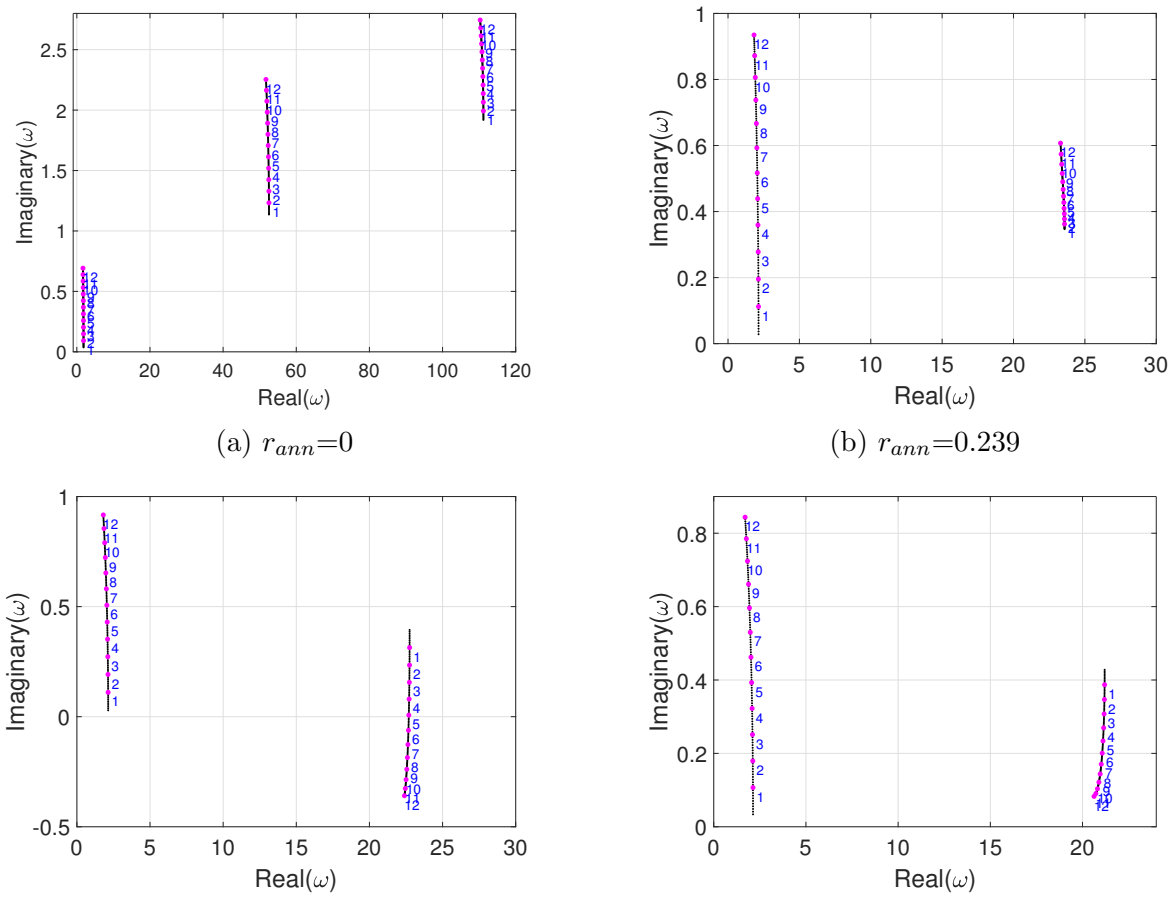

(a) r_{ann}=0 (b) r_{ann}=0.239

(c) r_{ann}=0.453 (d) r_{ann}=0.668

Figure 3–1: Theoretical Results:Effect of Confined Length Fraction r_{ann}

3.1.2 Effect of Cantilever Length

Several cantilever tube lengths (L) were tested, including 200 mm, 300 mm, 400 mm, 700 mm, and 1000 mm (Figure (3-2)). To isolate the effect of changing tube length, these tubes were unconfined with r_{ann}=0. Stability for all modes was observed. This implies that cantilever length does not affect the stability of the system.

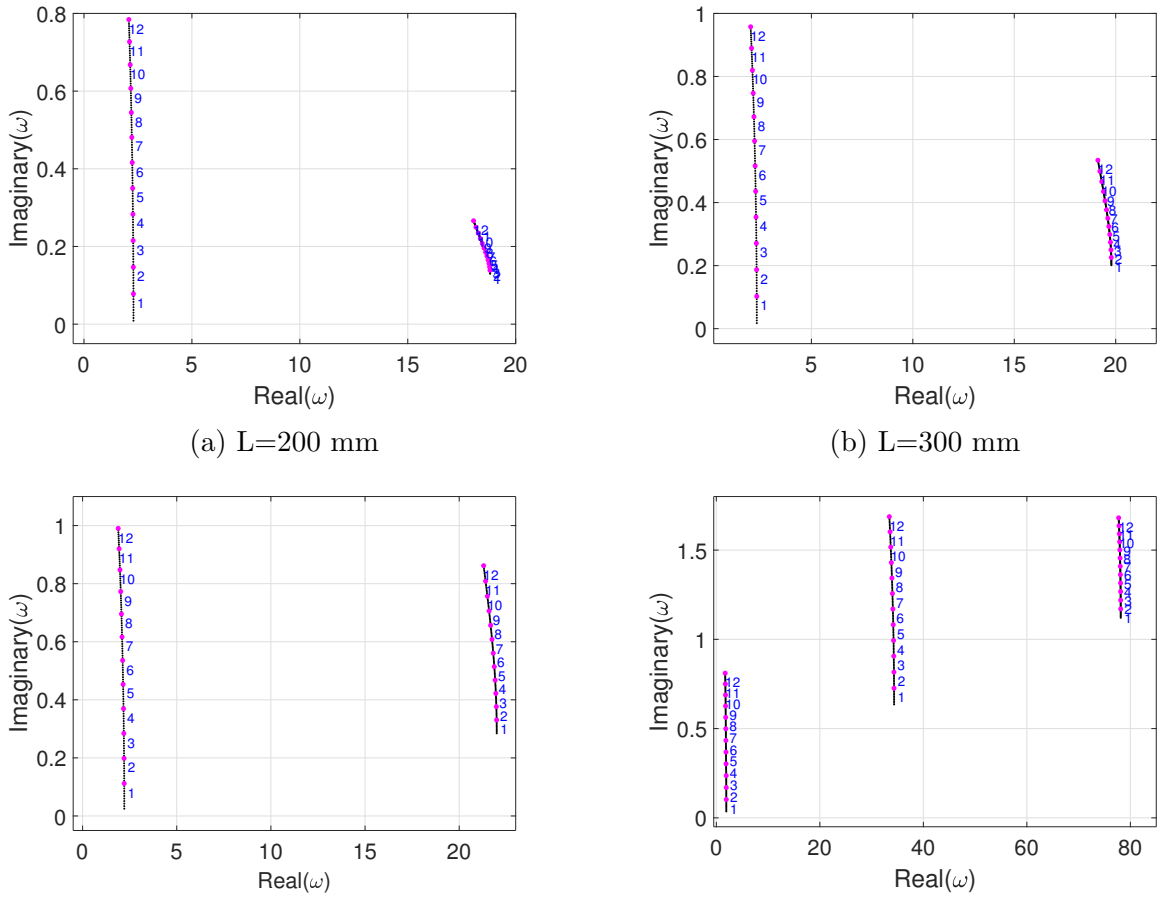

(a) L=200 mm

(b) L=300 mm

(c) L=400 mm

(d) L=700 mm

Figure 3–2: Theoretical Results:Effect of Tube Length L

3.1.3 Effect of End-mass

To see the effect of the mass of the end-piece on a pipe conveying fluid with discharging radial flow, the critical flow velocity is plotted as a function of the end-mass (Figure (3-3)). The mass of the end-piece was increased between 0 and 0.05 kg.

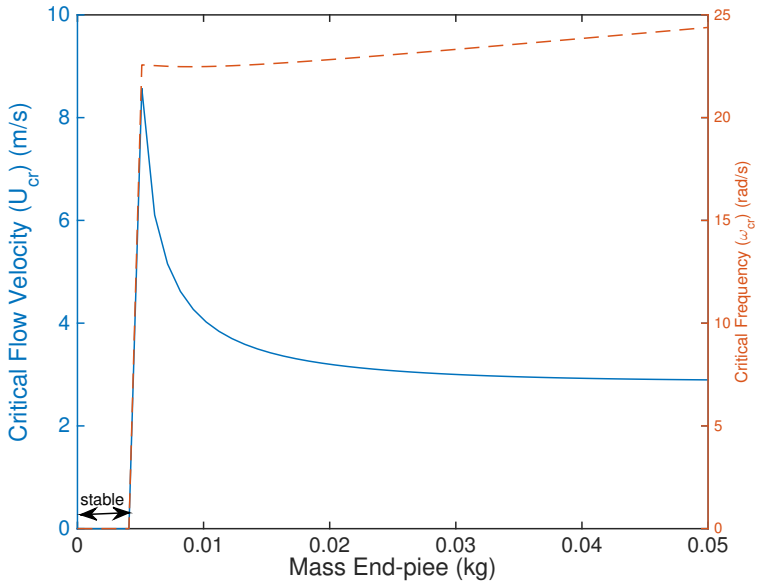

Figure 3–3: Theoretical Results: Effect of End-Mass m_e

If the mass of the end-piece is in the range of 0 to 0.004 kg, stability is predicted. As the mass of the end-piece is increased to 0.005 kg, the cantilever loses stability by flutter for a critical flow velocity of 8.6 m/s. Beyond this range, the critical flow velocity for flutter is decreased. Thus, the cantilever is destabilized as the mass of the end-piece is increased.

3.1.4 Theoretical Results for Brine-string parameters

Theoretical radial flow results are presented for long brine-string systems, such as those used in industrial applications and salt-cavern hydrocarbon storage. Typical dimensional and non-dimensional parameters for brine-string systems are defined in Table 3-1. In the industrial application, salt-cavern operators have some flexibility in varying parameters, including a_{ch}, r_{ann}, L, and m_e. In the subsequent sections, each

of these parameters is varied to see their effect. For each case, stability was assessed for increasing internal flow velocity U_i varying from 0 to 30 m/s. A minimum of 11 modes are used in each case, and only the first instability with increasing flow is reported.

3.1.5 Effect of Confinement α_{ch}: Brine-string parameters

The effect of varying a_{ch} on brine-string systems is discussed here. This parameter, a_{ch}, is the ratio between the channel diameter (D_{ch}) and the outer diameter of the cantilever (D_o). Thus, larger values of a_{ch} correspond to a wider channel and a decrease in the annular flow velocity U_o. The results shown here are based on L=200 m, m_e=1000 kg, and r_{ann}=0.50. The parameter a_{ch} was varied from 1.1 to 20. For very narrow channels or a_{ch} ranging between 1.1 and 1.42, the cantilever loses stability by first-mode flutter, with the critical flow velocity (U_{cr}) increasing from 0.25 to 9.98 m/s and the critical frequency (ω_{cr}) decreasing (Figure (3-4)). As the channel widens, for a_{ch} from 1.43 to 1.8, ω_{cr} drops to 0, indicating buckling or static divergence instability. The critical flow velocity increases steadily from 10.4 m/s to 26.2 m/s, indicating a stabilization effect for the channel widening. Further increase in channel diameter resulted in complete stability in all modes for a_{ch} between 1.9 and 20.

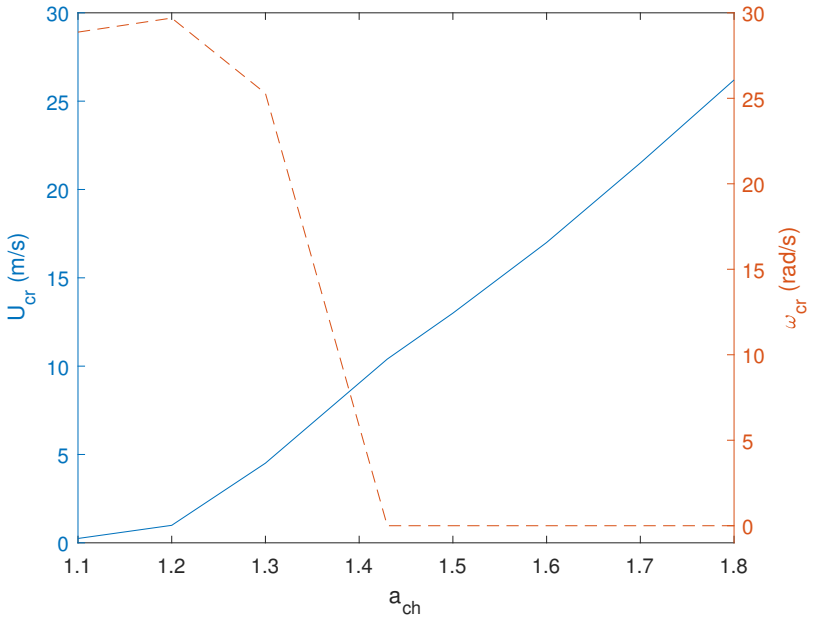

Figure 3–4: Theoretical Results: Drill-String Parameters:Effect of α_{ch}

3.1.6 Effect of Confined Length Fraction r_{ann}: Brine-string parameters

The effect of the confined length fraction or ratio between the length of the rigid outer tube (L') and cantilever length (L) was investigated. Larger values of r_{ann} signify a larger percentage of the cantilever is subjected to annular flow. Theoretical results for the brine-string system are presented in Figure (3-5) . For this investigation, two brine-string lengths were considered, L=100 m and L=200 m. A value of 1.676 was used for a_{ch} (a common value used in real life application) and m_e was set to 0.

For the 100 m length drill-string, Figure (3-5a), r_{ann} was given the following values: r_{ann}=[0; 0.125; 0.15; 0.25; 0.47; 0.50; 0.6875; 0.70; 0.75; 0.85]. The drill-string showed stability for $r_{ann} < 0.25$. For r_{ann}=0.25 first mode flutter is predicted.

A further increase in r_{ann} to 0.47 and above resulted in first-mode static divergence; the trend in this range showing a decrease in U_{cr} and ω_{cr}=0.

For the 200 m length drill-string, Figure (3-5b), r_{ann} was given the following values, r_{ann}=[0; 0.125; 0.15; 0.25; 0.5; 0.6875; 0.7; 0.75; 0.85; 0.875]. For r_{ann}=[0; 0.125, 0.15], no instability was detected. An increase in confined length fraction to 0.25 resulted in destabilization by first-mode flutter. Further increase in r_{ann} between 0.5 and 0.875, first-mode divergence was observed. In this range, a steady decline in U_{cr} was seen between r_{ann}=0.5 to r_{ann}=0.6875 and for r_{ann}=0.85 to r_{ann}=0.875. An increase in critical flow velocity was seen for r_{ann}=0.7 and 0.75.

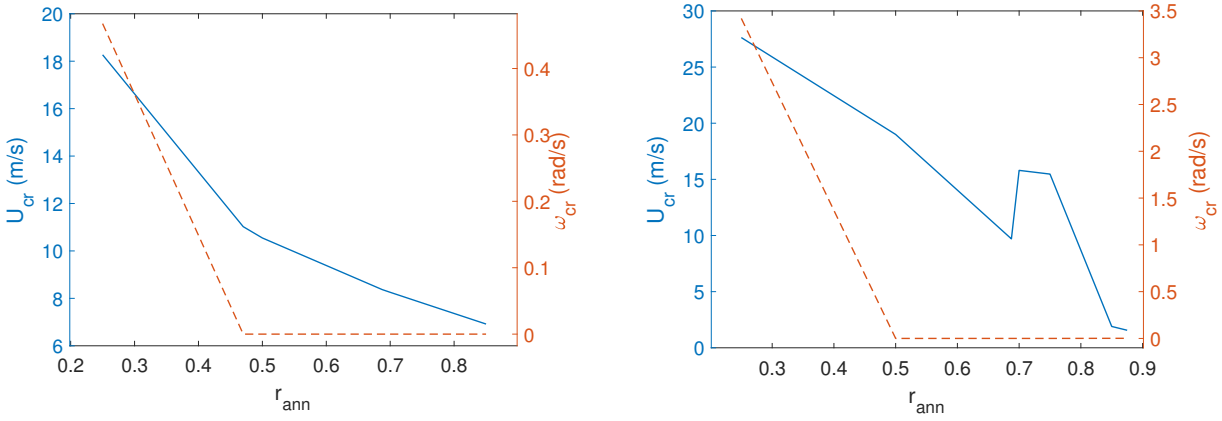

(a) L=100 m (b) L=200 m

Figure 3–5: Theoretical Results:Brine-String Parameters: Effect of r_{ann}

3.1.7 Effect of End-piece Mass m_e: Brine-string parameters

Experimentally, discharging radial flow was achieved through the use of an end-piece. If radial flow is to be implemented in a similar method to the bench-top scale system, an end-piece with a given mass would need to be added to block straight through flow and divert flow radially. This end-piece has a non-negligible weight

and can significantly impact the dynamics of the system; thus the theoretical model takes this mass into account. In this section, the end-piece mass was varied to see the effect on brine-string system stability. The end-mass parameter, m_e was increased from 0 to 500 kg for a drill-string length of 100 m and was increased from 0 to 1000 kg for a drill-string length of 200 m. This range was selected to be consistent with the experimental bench-top system parameters to maintain a similar ratio between end-piece mass and tube mass. Additionally, for both cantilever lengths, several values of r_{ann} were tested.

Stability was seen for the entire end-piece mass range for the 100 m length and the 200 m length cantilever for an unconfined drill-string or r_{ann}=0.

Drill-string legth 100 m: In Figure (3-6a), the cantilever length was 100 m and r_{ann}=0.125. The drill string did not demonstrate flutter or divergence for an end-mass between 0 and 76 kg. However, flutter instability is predicted for $m_e >$ 76 kg. In terms of critical flow velocity, the critical flow velocity is maximized for a mass of 76 kg and decays exponential for subsequent increase in mass.

In Figure (3-6b), r_{ann}=0.25 and the other parameters are kept the same. Static divergence occurs for end-piece masses between 0 and 61 kg, as evidenced by w_{cr}=0. As the end-piece mass is increased beyond 61 kg, flutter is predicted for an exponentially decreasing critical flow velocity. Further increasing r_{ann} to 0.50 results in similar behavior in which initially stability is lost by divergence which is then succeeded by flutter (Figure (3-6c)). In this case, for $0 \leq m_e \leq 316$ kg, static divergence is predicted and for $m_e > 316$ kg, flutter is predicted. Again, U_{cr} demonstrates an exponential decay like curve for large enough m_e.

In Figure (3-6d), for r_{ann} increased to 0.75, buckling instability is shown for a end-mass between 0 to 500 kg. In terms of critical flow velocity, U_{cr} is bounded between 7.8 and 8.45 m/s and increases with increasing mass.

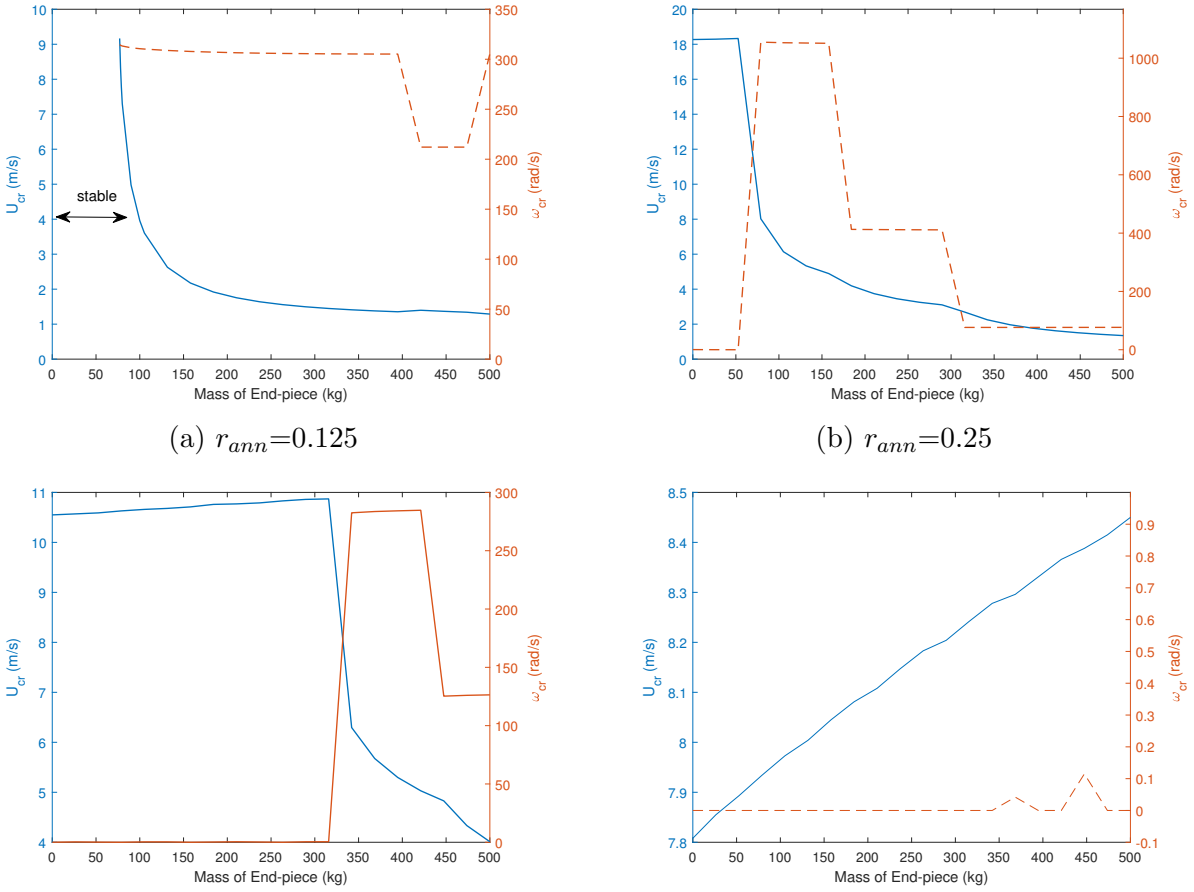

(a) r_{ann}=0.125

(b) r_{ann}=0.25

(c) r_{ann}=0.5

(d) r_{ann}=0.75

Figure 3–6: Theoretical Results:Drill-String Parameters:Effect of End-Piece Mass m_e for several r_{ann} L=100 m

Drill-string length 200 m:

For the longer, 200 m length system, the same confined length fractions are investigated for increasing end-piece mass from 0 to 1000 kg. Firstly, for r_{ann}=0.125, the cantilever is stable for $0 \leq m_e \leq 235$ kg. Subsequent increase in end-piece mass results in flutter for which the critical flow velocity starts at 14 m/s and asymptotically approaches 4 m/s . As seen in Figure (3-7a), w_{cr} shows a continuous rise for m_e >300 kg.

Figure (3-7b) shows u_{cr} and ω_{cr} for r_{ann}=0.25. As the mass is increased, the first type of instability seen is flutter (for $0 \leq m_e \leq 48$ kg), followed by buckling (for 49 kg $\leq m_e \leq$ 66 kg), and again flutter (for $m_e >$ 66 kg). The critical frequency for flutter starts around 4.5 rad/s, increases sharply, and finally stabilizes around 580 rad/s.

For r_{ann}=0.50, the drill-string is unstable by static divergence (ω_{cr}=0) for the entire mass range (Figure (3-7c)). The critical flow velocity remains between 19 and 20.4 m/s, with a general increase in flow velocity for increasing mass, indicating a stabilizing effect.

The 200 mm cantilever system with the highest confined length fraction, r_{ann}=0.75 also displayed static divergence for the entire mass range. In this case, U_{cr} ranged between 15.47 and 16.54 m/s, and displayed an increasing trend for increasing end-mass (Figure (3-7d)).

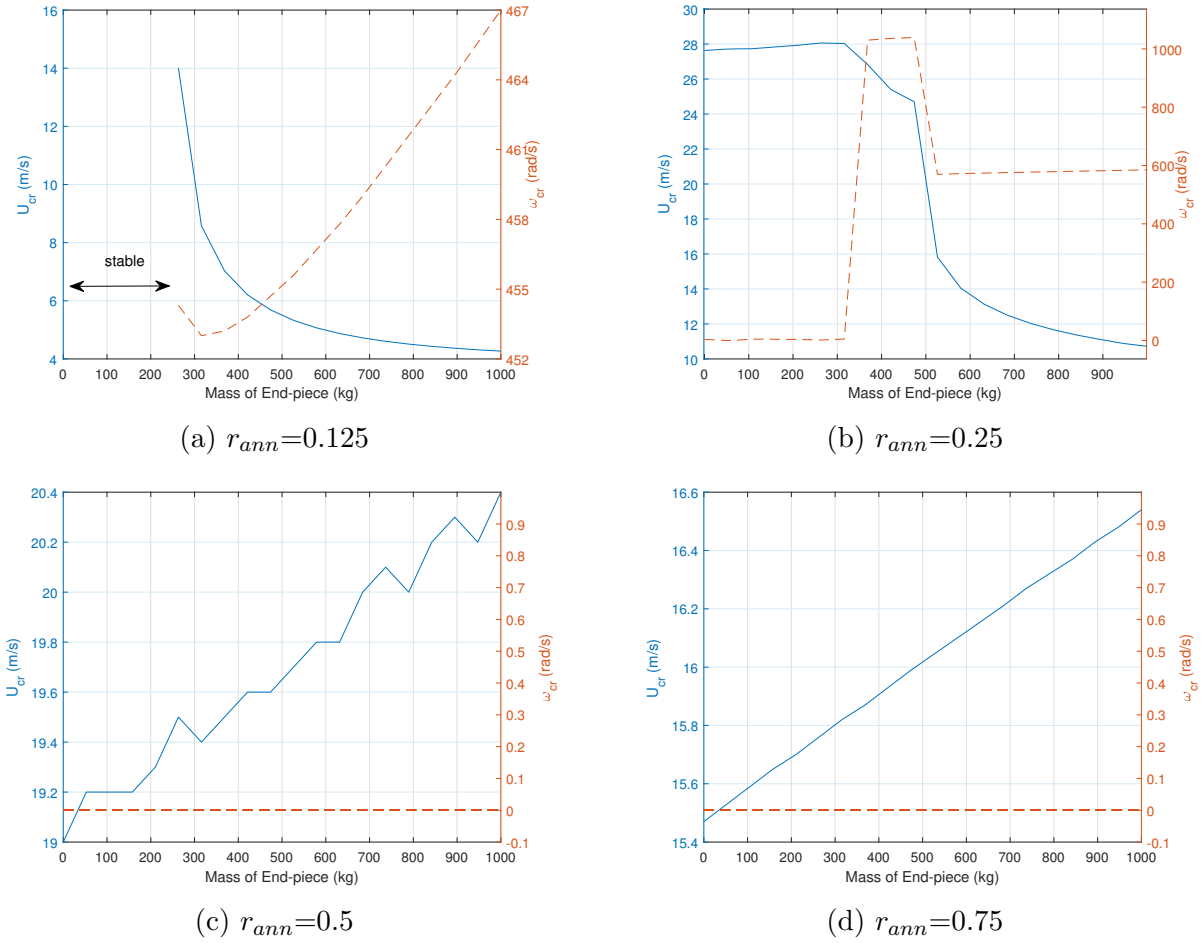

(a) r_{ann}=0.125

(b) r_{ann}=0.25

(c) r_{ann}=0.5

(d) r_{ann}=0.75

Figure 3–7: Theoretical Results:Drill-String Parameters:Effect of End-Piece Mass m_e for several r_{ann} L=200 m

3.1.8 Stability with Brine-string parameters: The effect of radial flow

The results presented previously indicate a combination of parameters for which the drill-string system discharging flow radially is stable and hence not demonstrating divergence or flutter. In addition to these results, further analyses were completed to further investigate combinations for stability. The following tables, 3–2 and 3–3

indicate values for r_{ann}, m_e, and α_{ch}, for which the drill-string is stable. This was accomplished for two drill-string lengths, 100 m and 200 m.

Table 3–2: Parameters for Stability: Drill String System L=200 m

r_{ann}	m_e [kg]	α_{ch}
0	0 –1000	1.676
0.125	0 – 235	1.676
0.125	0 – 715	≥ 2
0.25	0 – 1000	≥ 1.9
0.5	0 – 1000	≥ 1.9
0.75	0 – 1000	≥ 2.7

Table 3–3: Parameters for Stability: Drill String System L=100 m

r_{ann}	m_e [kg]	α_{ch}
0	0 –500	1.676
0.125	0 – 76	1.676
0.125	0 – 363	≥ 2.4
0.25	0 – 493	≥ 2.4
0.5	0 – 500	≥ 2.4
0.75	0 – 500	≥ 2.6

CHAPTER 4
Experiments

Experiments were performed in the Solution Mining Research Institute (SMRI) pressure vessel in the Fluid-Structure Interactions Laboratory of McGill University. This pressure vessel represents a scaled down model of the brine-string and casing found in salt cavern hydrocarbon storage applications. The pressure vessel consists of a stainless steel chamber, a flexible rubber tube used to simulate the brine-strings, and a larger diameter rigid tube used to simulate the casing. An annulus is formed in the space between the flexible tube and the rigid outer tube, allowing for annular flow.

For configuration (iii) experiments, flow is directed from the clamped end of the tube to the free end discharging either axially or radially (depending on the end-piece used); the flow is then re-directed into the annular space, aspirating towards the clamped end (Figure (4–2c)).

For configuration (iv) experiments, flow is discharged through the annular space, re-directed and aspirated either axially or radially (depending on the end-piece used); through the free end of the hanging cantilever (Figure (4–2c)).

The pressure vessel is filled and operated with water as the working fluid. Motion capture of the free end of flexible cantilever tube is completed with an Optron vibrometer system as well as a dual camera system.

4.1 Experimental Apparatus

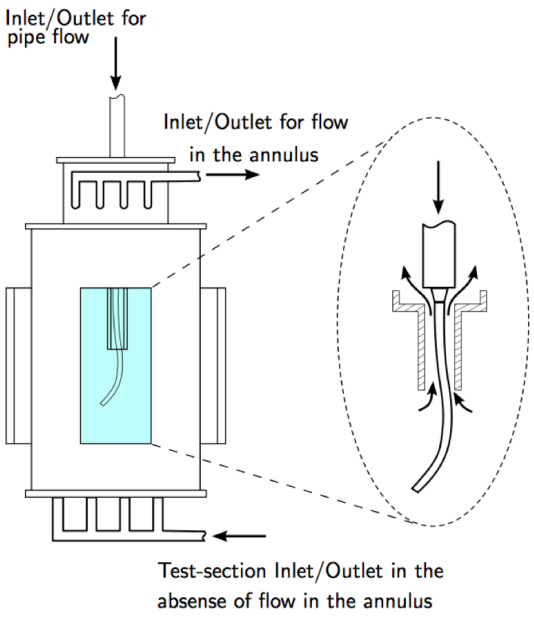

Figure 4–1: Pressure Vessel

4.1.1 Pressure Vessel

The experimental apparatus consists of a stainless steel cylindrical pressure vessel that is 0.6 m tall by 0.48 m internal diameter (Figure(4-1)). The pressure vessel has four rectangular viewing windows, positioned at right angles to one another. Pressures up to 45 psi can be sustained in this vessel, limiting the maximum attainable flow velocity. To de-aerate the system, two manual bleed valves are used when filling the chamber and in-between data recording.

The pressure vessel is filled and flow velocity through the pipe is varied through the use of a 2.2 kW electric centrifugal pump. The gain on the pump is controlled by digital controllers and is manually adjusted during experimentation to adjust the flow rate. The pump is supplied water from a large water holding tank.

4.1.2 Flexible Tubes

Flexible tubes made of Silastic RTV (two-part silicone) were cast and used experimentally to simulate the brine string (Figure (4–2a)). The flexible tube is secured to the top of the pressure vessel.

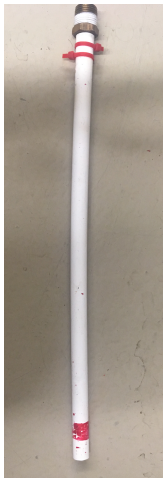

(a) Flexible Cantilever Tube

(b) Annuli

(c) Radial Flow End-piece with 4 Holes

Figure 4–2: Experimental Materials

4.1.3 Annulus

The casing of the brine-string system was simulated using rigid, transparent Plexiglas tubes of larger diameter with respect to the the flexible tube. These rigid outer tubes had an internal diameter or D_{ch}=31.5 mm and varied in length. Three annuli of nominal length 100 mm, 200 mm, and 300 mm were used (Figure (4–2b)).

These rigid outer tubes were secured to the top of the pressure vessel, concentrically surrounding the flexible tube. An annulus is formed in the space between the rigid and flexible concentric tubes, in which water can flow external to the flexible tube.

4.1.4 Schematic of System

There is one inlet and one outlet into the pressure vessel, and no accumulation of water into the system as water is recycled through the water tank.

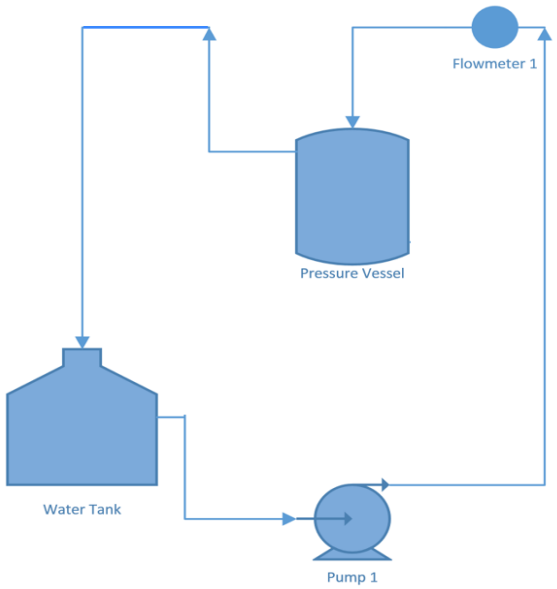

Figure 4–3: Schematic of the System

4.2 Data Acquisition

4.2.1 Flow-rate

A Rosemount magnetic flow-meter system, integrated with a display was used to measure the internal flow velocity in the flexible tube. The flow-meter output

was measured in liters per second with a resolution of 0.001 Lt/s. Flow rate adjustments were made by changing the pump gain and observing the volumetric flow rate displayed on the flow meter.

4.2.2 Motion Capture

Optron: Motion of the free end of the flexible tube was measured through the use of an Optron 5600 which is an analog single-point vibrometer. It was positioned in front of one of four viewing windows of the pressure vessel. The Optron 5600 is similar to camera in that it captures motion in a plane perpendicular to the axis of the device. It outputs a voltage signal proportional to the displacement of a tracked point on the free end of the pipe. To calibrate, a voltage-displacement curve was made to convert the voltage output to displacement data.

Dual Cameras: The movement of the free end of the pipe was also tracked at each flow velocity point using high speed cameras. Two cameras were used to capture the movement of a target strip (about an inch in length) on the pipe free end. These cameras were positioned perpendicularly to each other and at the same height, with one camera viewing the target from the front window and one camera viewing from a side window. The dual camera system was considered to be an improvement as compared to the Optron, as movement was captured in two planes instead of only one. For static deflections of the free end of the tube, the dual cameras were absolutely necessary to really capture the position of the tube, as in some cases, deflections occurred at an angle between the two windows. While the Optron could only view defections from the perspective of one window, the dual cameras could capture the

full motion, giving a much more accurate depiction. All experiments were completed with both the Optron and the dual cameras for verification of the results.

4.2.3 Pressure Measurement

A Bourdon tube gage installed on the bleed line, before the manual bleed valve was used to measure the pressure in the pressure-vessel. Pressure readings were monitored to ensure pressures did not exceed 45 psi to prevent leaks and potential damage to the experimental apparatus.

4.3 Experimental Procedure

1. Depending on the configuration, piping is adjusted to change the inlet/outlet of the system.
2. The flexible tube was painted with a dark, one inch strip around the outer surface of the tube. This was only done for data capture with the dual cameras.
3. The front window of the pressure vessel is removed, allowing for installation of the specimen. The flexible tube and annulus were installed to the top of the pressure vessel; both are adjusted to ensure concentricity and verticality.
4. The front window was then re-installed, using vacuum grease to prevent leaks through the window.
5. The pressure vessel was filled with water, pressurized, and then run for about 1 hour to de-aerate the system.
6. (a) **Optron:** The Optron 5600 was leveled and positioned to track a point very close to the free end of the pipe. Since the Optron uses light luminosity contrast to track movements, the light levels of a light positioned

behind the specimen were adjusted to obtain the required contrast. Once the light levels were adjusted and tracking established, the Optron was calibrated by producing a voltage vs. displacement curve.

(b) **Dual Cameras:** The dual cameras were positioned in front of perpendicular windows, the same distance from the windows and at the came height. Lamps positioned in between the cameras and its respective window were used to create the proper light contrast. The camera settings were configured to focus on the dark target strip, one inch in length that was painted on very close to the free end of the tube.

7. The pump was then turned on, and gain adjusted to reach the desired flow velocity.

8. (a) **Optron:** Data was recorded for 500 seconds at a sampling rate of 2048 for each flow velocity point.

   (b) **Dual Cameras:** H264 video data was recorded for 200 or 800 seconds (depending on the experiment) and with a frame rate of 64 frames/second.

4.4 Data Analysis

For each internal flow velocity point recorded, the Optron produced one data set from one of the side windows. The dual camera system produced two data sets, one from a side window and one from the front window.

Different methods were used to extract the raw displacement data from the Optron and the dual cameras. Raw voltage data, outputted from the Optron was converted to displacement data using the calibration curve. However, for the dual camera system, a separate Matlab script was used to extract the displacement data.

The centroid of the area of the painted markers was calculated and used as the representative position of the tube for each frame. The tube displacement was calculated by subtracting the centroid location from the tube location at zero internal flow velocity.

Further data analysis was completed using another Matlab script that was the same for both motion capture systems.

Taking the raw displacement data, this data was normalized by subtracting mean displacements from the raw displacement data. The normalized displacements were plotted against time to produce a standard time series curve to help visualize general system motion. The time series data was smoothed using a finite impulse response (FIR) filter in Matlab. The root-mean-square (rms) of the displacement data was calculated in order to visualize dynamic system behavior. The onset of oscillatory instability can be viewed graphically from an rms amplitude vs. internal flow velocity curve, as a sudden increase in rms amplitude.

The vibration frequencies of the flexible tube were calculated by computing the Power Spectral Density (PSD). The PSDs were calculated and compared with two methods: fast Fourier transform (FFT) and Welch's method with eight windows. The dominant peak present in these curves was identified as the vibration frequency.

CHAPTER 5
Experimental Results: Radial Flow

5.1 Experimental Results for Configuration (iv): Pipe aspirating fluid; the annulus discharging fluid

Several experiments for configuration (iv) were conducted for a Silastic tube fitted with a 200 mm plexiglas rigid tube. For this set of experiments, Delrin plastic end-pieces were fitted to the free end of the cantilever tube. These end-pieces include one with 4 radial holes (diameter 0.25 in) and one with 8 radial holes (diameter 0.125 in). The diameter of the axial hole present in all of the end-pieces is 0.25 in, which is the same as the interior diameter of the flexible tube.

Results for partially-confined, discharging, cantilever pipe with reverse external flow are discussed and compared for axial and radial discharge configurations. From the extracted displacement data, time series plots, rms amplitude plots, and PSD plots are analyzed and compared.

5.1.1 Comparison of Experimental Results for Configuration (iv)

A flexible hanging cantilever aspirating flow axially and radially demonstrates the same behavior. This is further verified through analysis of the displacement data including time series plots, rms amplitudes, and PSD plots.

Visually, the tube lost stability by first-mode flutter for a low critical flow velocity. Beyond the onset of first-mode flutter, further increase in flow velocity resulted in the emergence of first-mode flutter and second-mode flutter simultaneously. At high

enough flows, movement of the tube can be characterized as full three-dimensional motion, with the amplitude of this motion increasing with increasing flow velocity. It should also be noted that when flow velocity was increased beyond points of instability, impacting or contact between the flexible tube and an interior surface of the rigid tube occurred. Again, this is consistent for both axial and radial flows.

Rms Amplitude Comparison:

Graphically, the rms amplitude (mm) vs. internal flow velocity of the pipe (m/s) was compared for each of the cases. The rms amplitude was taken as the displacement of the free end of the pipe and helps characterize the average movement of the pipe end. Referring to Figure (5–1), data is given for a cantilever without an end-piece, a cantilever with a 4 holes end-piece, an 8 holes end-piece, and an axial end-piece.

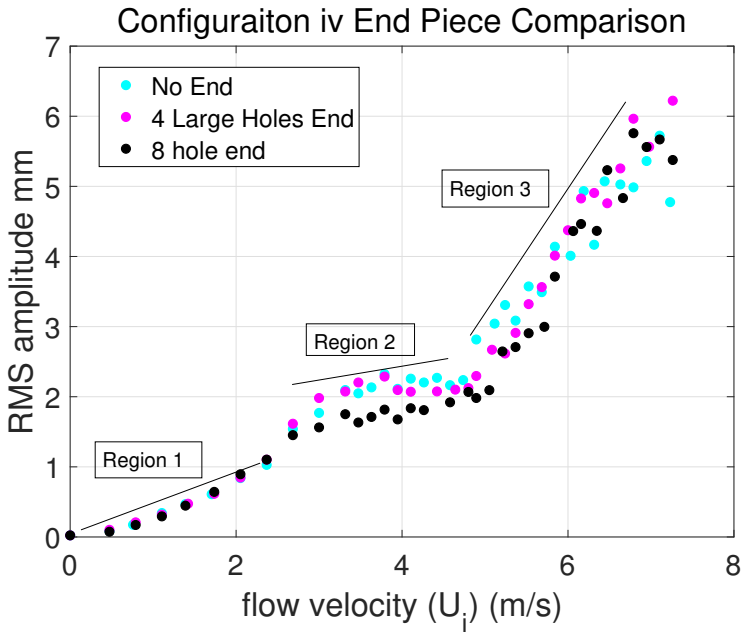

Figure 5–1: Rms:Configuration (iv) Axial and Radial Flow

For clarity, three regions are defined, based on internal flow velocity U_i, Region 1 (0-2.5 m/s), Region 2 (2.5-5 m/s), and Region 3 (5-7.5 m/s). In Region 1, all of the curves are the same, with indiscernible differences in the data points. In Region 2, all of the curves show the same pattern as the flow velocity and pipe movement increases. For this region, the 8 holes end-piece exhibited slightly less pipe movement as compared to the other end-piece arrangements. In Region 3, curves have a similar slope with points in each of the curves showing deviations from the general trend (at flow velocities between 6.8 and 7.5 m/s) likely due to impacting. The critical flow velocities U_{cr} for first-mode flutter and second-mode flutter were demonstrated as the flow velocity for which there is a sudden increase in rms amplitude. According to Figure (5-1), for all three cases, this occurs at flow velocity of 3.5 m/s for first-mode flutter and 5 m/s for second mode flutter.

In general, the various end-piece arrangements show marginal differences in pipe movement and stability visually as well as graphically. This implies that for configuration (iv) radial entry flow does not affect system behavior.

Time Series Comparison:

The time series for both axially and radially discharging flow show similar behavior. As seen in the displacement-time series plots, segments of nearly periodic motion are present. Between these segments of periodic motion are periods of smaller amplitude motion that resemble 'shuddering' or quasi-chaotic motion. As flow velocity is increased, the periodic motion can become slightly distorted and segments of small amplitude motion increase in amplitude for higher flows.

Low flow: For an internal flow velocity between 0.5 and 2 m/s, periodic-like motion is seen in the displacement time series. This motion is low in amplitude, on the order of 2 mm.

For internal flow velocities between 2 and 5 m/s, periodic-like motion is still present. However, the amplitude of this motion is increased. Between segments of periodic motion are periods of shuddering or quasi-chaotic motion, which are of lower amplitude.

High flow: For flows beyond the point of instability ($U_i > 5$ m/s), the displacement amplitude is increased for the periodic-like motion and for the shuddering motion (Figure (5–2)).

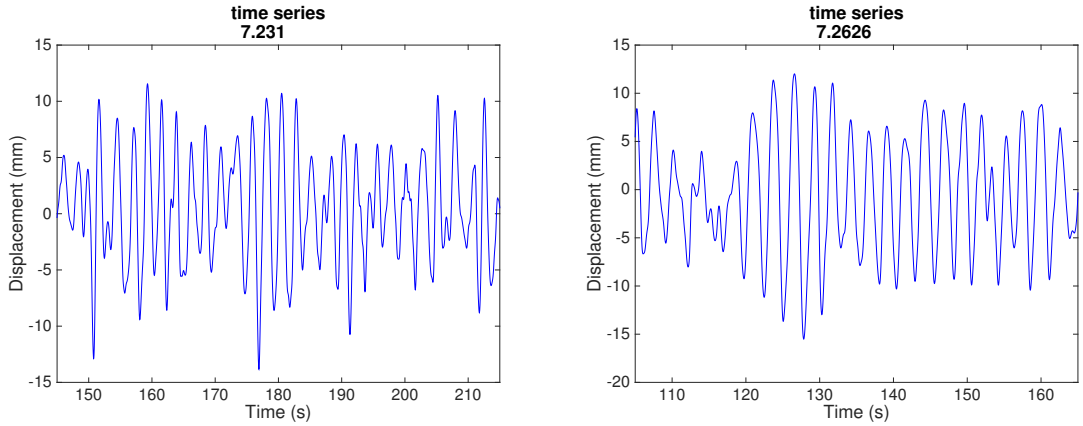

(a) Axial Flow (b) Radial Flow

Figure 5–2: Time Series: Configuration (iv)

Frequency Comparison:

The frequency results for all variations in configuration (iv) were very similar. Power Spectral Density (PSD) and Fast Fourier Transform (FFT) were calculated

from the recorded displacement-time series data. Peaks in these graphs correspond to dominant frequencies in the system (Figure (5–3)).

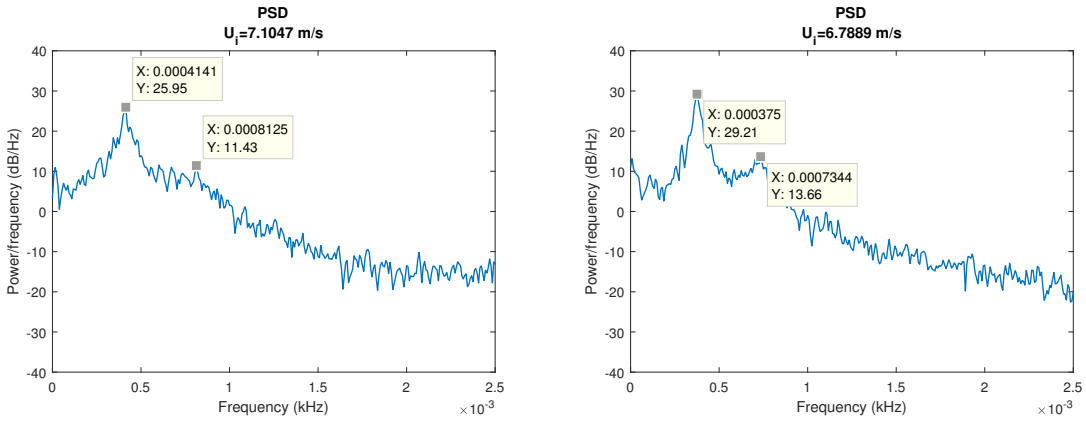

(a) Axial Flow (b) Radial Flow

Figure 5–3: PSD: Configuration (iv)

The behavior for configuration (iv) can be characterized as follows. For low flow velocity, below 3 m/s, one dominant frequency peak is observed, corresponding to the first mode of vibration of the cantilever. Between roughly 3 and 7.5 m/s a second dominant peak can be clearly identified in Figure (5–3), with the second frequency peak corresponding to the second mode of vibration.

5.1.2 Conclusions of Experimental Results for Configuration (iv)

Behavior and stability of an aspirating cantilever was the same for flow entering axially or radially. The tube loses stability by first-mode flutter for critical flow velocity U_{cr} of 3 m/s, and 5 m/s for second mode flutter. Beyond the onset of first-mode flutter, further increase in flow velocity resulted in the emergence of first-mode flutter and second-mode flutter simultaneously. This is consistent with the PSD of the signal in which two peaks become evident for higher flow velocities.Thus at high

enough flows, movement of the tube can be characterized as full, three-dimensional motion, with the amplitude of this motion increasing with increasing flow velocity. As shown in the displacement-time series plots, as the flow velocity is increased, the amplitude of periodic-like motion and 'shuddering' is increased. This is consistent with the increase in rms amplitudes for higher flows.

5.2 Configuration (iii) Radial Flow Experiments

Several experiments for configuration (iii) were conducted for a 456 mm Silastic tube fitted with an internal diameter of 6.35 mm and an external diameter of 16 mm. For these experiments, plastic end-pieces were fitted to the free end of the cantilever tube to divert the flow out radially from the free end of the tube. Several end-pieces were used: with 4 large radial holes (diameter 6.35 mm x 4), 4 medium radial holes (diameter 4.7625 mm x 4), 4 small radial holes (diameter 3.175 mm x 4), 2 radial holes (diameter 6.35 mm x 2). The diameter of the axial hole present in all of the end-pieces was 6.35 mm, which is the same as the interior diameter of the flexible tube.

The effect of confined length fraction, pipe length, exit flow area, end-piece balance, end-piece orientation, and radial flow were experimentally investigated.

5.2.1 Comparison of Experimental Results for Configuration (iii)

Axial flow results for straight through flow through the tube are compared to discharging radial flow results for internal flow velocity increasing from 0 to 7.5 m/s.

Axial Flow: For a cantilever discharging axial flow, the flexible tube displayed very little motion for low flow velocities. As the flow velocity was increased, the flexible tube lost stability by second-mode flutter for high enough flows.

Radial Flow: For cantilevers discharging flow radially, the tube displayed very little motion for the entire flow velocity range. For radial flow, flutter ceased and stability of the tube was observed. However, static displacement of the tube occurred (likely due to geometric imperfections in the end-piece). As the internal flow velocity was increased, static bending of the flexible tube was observed in which the unconfined portion of the tube diverged increasingly from the vertical axis, and in some cases made contact with the outer rigid tube.

Rms Amplitude Comparison: The rms amplitude was calculated from normalized displacement data to observe vibration amplitude and to calculate a critical flow velocity. This was done for axial flow and radial flow, allowing for comparison. The onset of instability can be determined from rms amplitude plotted against internal flow velocity. A sudden increase in rms amplitude indicates an onset of oscillatory instability. According to this curve (Figure (5–4)), a sudden increase in slope of the curve occurs around 5 m/s, which is the critical flow velocity (U_{cr}) marking the onset second-mode flutter, for discharging axial flow.

For discharging radial flow, rms of the normalized displacement data showed negligible vibration over the entire internal flow velocity range. As seen in Figure (5–4), the rms amplitude is less than 0.14 mm.

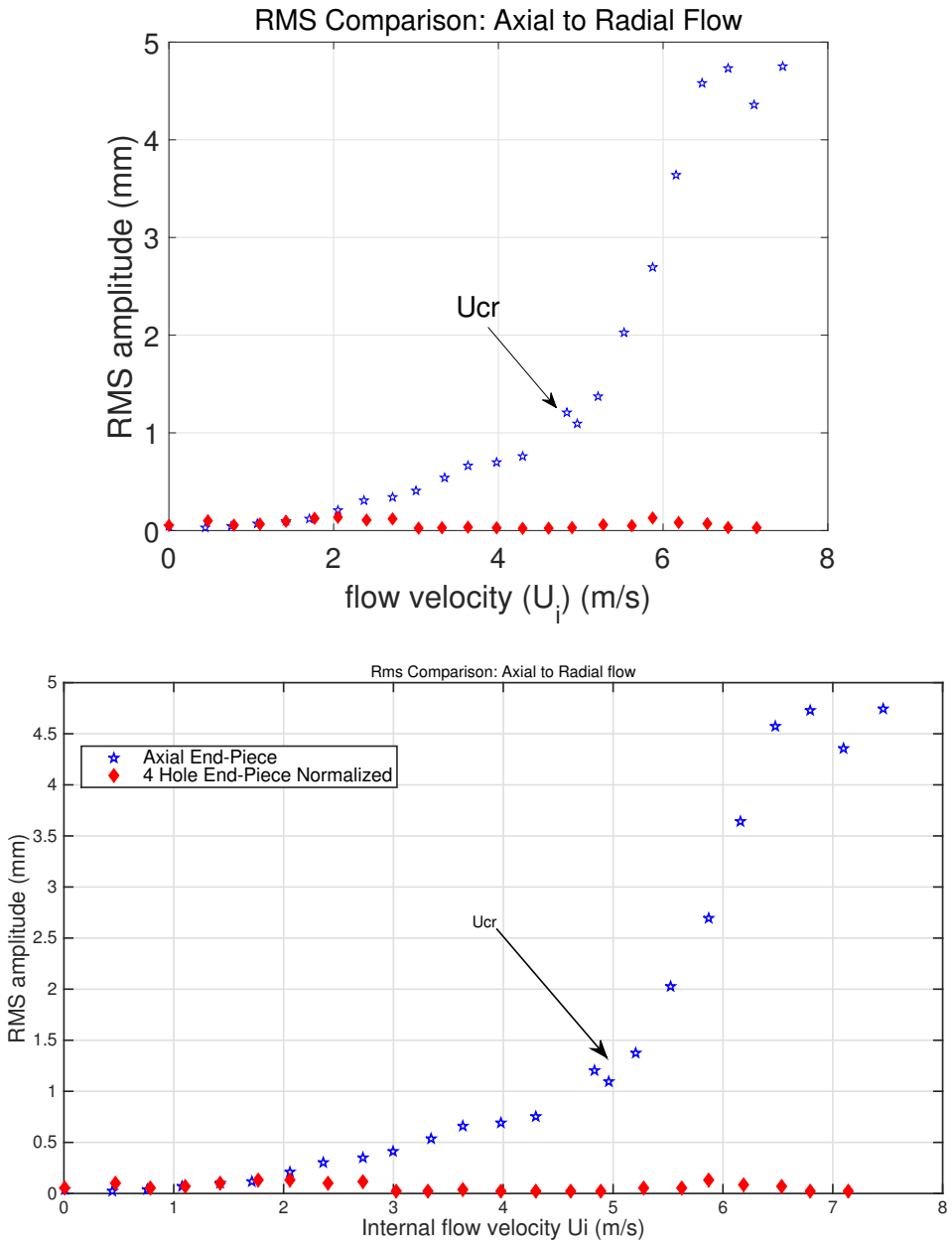

Figure 5–4: Rms: Configuration (iii) Axial vs. Radial Flow Comparison

Time Series Comparison: Axial flow: As seen in the displacement-time series plots (Figure (5–5a)), segments of periodic motion are present. Between these segments of periodic motion, are periods of smaller-amplitude motion. As the flow velocity is increased, the periodic motion can become slightly distorted and segments of small amplitude motion increase in amplitude for higher flows.

Radial flow: Only extremely small amplitude oscillatory motion is present for the highest flow velocities (Figure (5–5b)). It can be concluded that the tube is stable, as such oscillations are considered negligible.

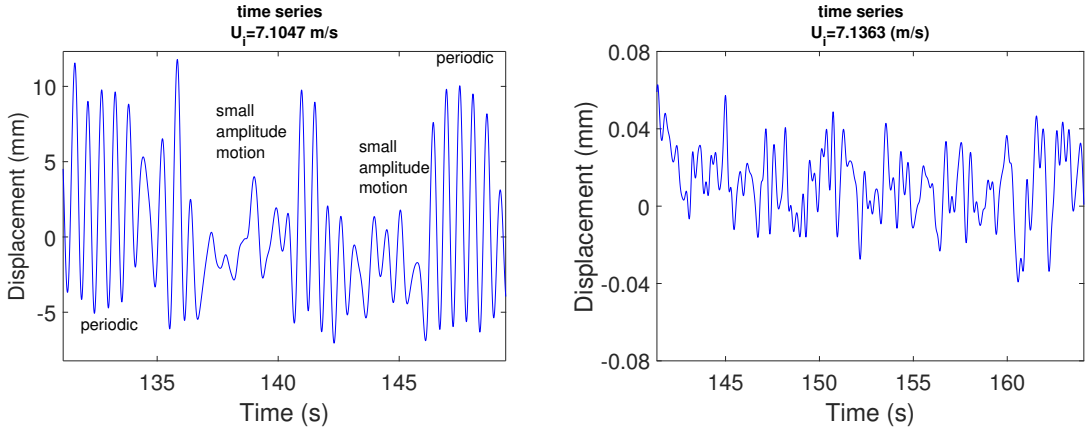

(a) Axial Flow: U_i=7 m/s (b) Radial Flow: U_i=7 m/s

Figure 5–5: Time Series: Configuration (iii) Axial vs. Radial Flow Comparison

Frequency Comparison: A dominant frequency of 1.6 Hz is present for discharging axial flow (Figure (5–6)). However, since the tube discharging radial flow is essentially static, a dominant frequency is not resolved in this case.

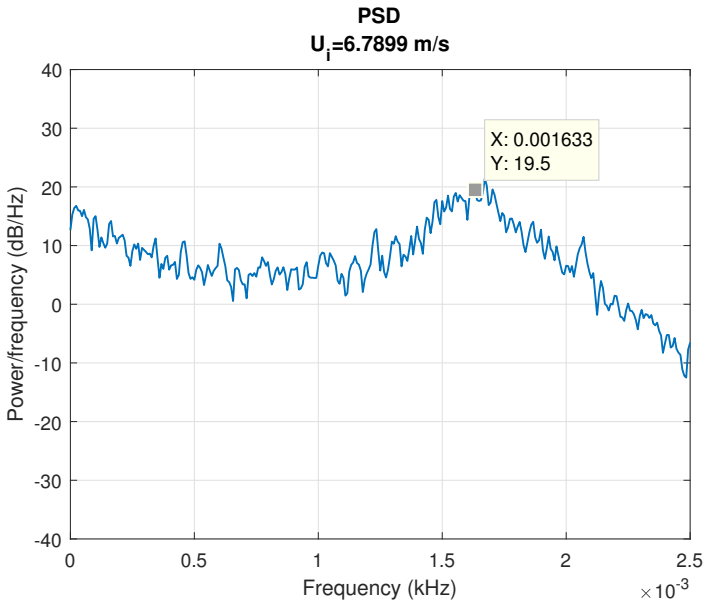

Figure 5–6: PSD: Configuration (iii) Axial Flow

5.2.2 The Effect of Confined Length Fraction

The 456 mm Silastic tube was fitted with the 4 large hole end-piece for radial flow. Several rigid outer tube lengths were explored, including: 0 mm (unconfined tube), 109 mm, 206.5 mm, and 304.5 mm or in terms of confined length fraction (r_{ann}): 0, 0.239, 0.453, and 0.668. Figure (5–7) shows the magnitude of the pipe movement at the free end. To compute the displacement magnitude (in mm), the lateral movement of the pipe recorded from the cameras at each flow velocity point was subtracted from the pipe position at zero internal flow velocity. An average was then taken. The lateral displacement data from the two cameras was then combined using the square root of the sum of the squares to show the displacement magnitude. This was then plotted against internal flow velocity (U_i). As shown in Figure (5-7),

as internal flow velocity is increased, the displacement magnitude is also increased, in a parabolic fashion.

With no outer rigid tube (0 mm), at 4 m/s, the maximum displacement observed was 90.5 mm. At 2 m/s, the displacement magnitude was 20 mm. The curve shows a parabolic shape, demonstrating how static deflection of the free end increases with increasing internal flow. Displacement of the free end of the pipe starts around 0.5 m/s of internal flow.

For r_{ann}=0.239, at 2 m/s, the displacement magnitude was 20 mm. Again, movement of the free end starts at 0.5 m/s of internal flow and for increasing flow, a parabolic displacement curve is seen (Figure (5–7))).

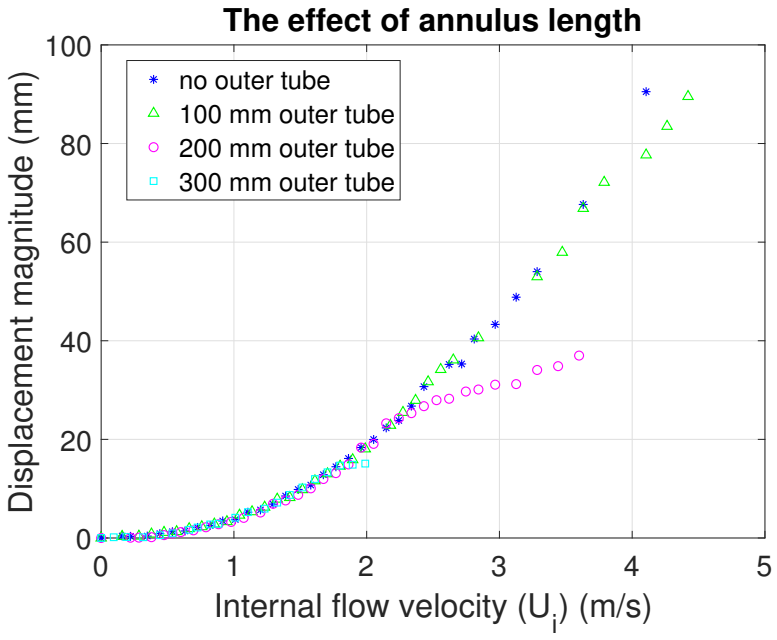

Figure 5–7: Experimental Results: Configuration (iii): Effect of r_{ann}

For r_{ann}=0.453, at 2 m/s, the displacement magnitude was close to 20 mm. Again, movement of the free end starts at 0.5 m/s of internal flow and for increasing flow, a parabolic displacement curve is seen between 0 and 2.5 m/s. The flexible tube makes contact with the outer rigid tube for an internal flow velocity of 2.5 m/s. This explains the change in parabolic behavior seen for 2.5 to 3.6 m/s.

For r_{ann}=0.668, movement of the free end starts at 0.5 m/s of internal flow and for increasing flow, a parabolic displacement curve is seen between 0 and 1.8 m/s. The flexible tube makes contact with the outer rigid tube for an internal flow velocity of 1.9 m/s. This explains the change in parabolic behavior seen for 1.9 to 2 m/s.

5.2.3 The Effect of Tube Length

Several pipe lengths fitted with the 4 large radial hole end-piece were tested. The tube was cut to lengths of 400 mm, to 300 mm, to 200 mm. For each tube length investigated, static deflection occurred around 0.5 m/s internal flow velocity, with displacement magnitude increasing parabolically with respect to increasing internal flow velocity. The displacement magnitude decreased for decreasing tube length (Figure (5–8)). To compare for example, for an internal flow velocity of 1.48 m/s, the 200 mm pipe showed a displacement magnitude of 1.14 mm. For the same internal flow velocity, the 300 mm pipe displacement was 3.19 mm, and for the 400 mm pipe the displacement was 12.27 mm.

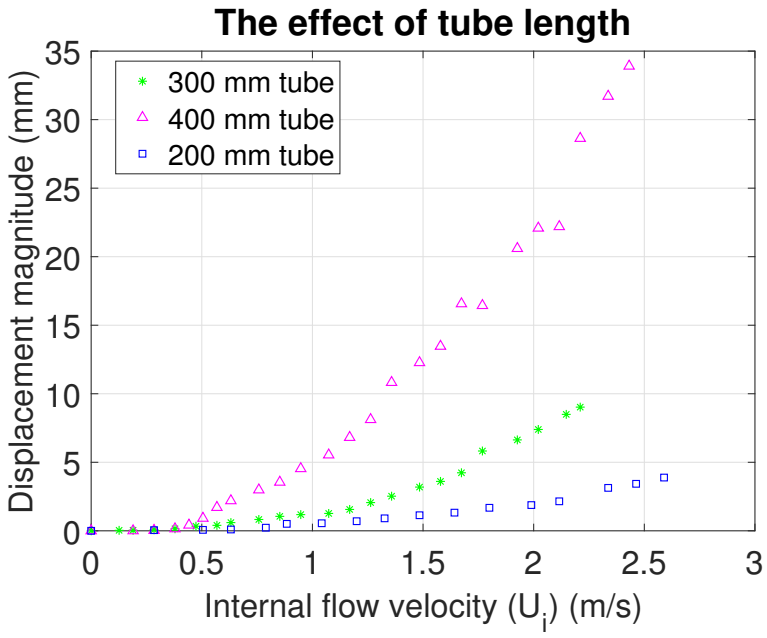

Figure 5–8: Experimental Results: Configuration (iii): Effect of Tube Length (L)

5.2.4 The Effect of Flow Area

On a 456 mm pipe, several end-pieces with different sized holes were tested experimentally to see the effect of flow area on displacement magnitude. Three end-pieces were tested with 4 radial holes: 4 large holes (diameter 6.35 mm), 4 medium holes (diameter 4.7625 mm), and 4 small holes (diameter 3.175 mm). Due to the different sized holes, the exit flow velocity from the cantilever free end is different for each end-piece. The 4 large hole end-piece has the largest flow area and thus the smallest exit flow velocity. Figure (5–9) shows the following trend, when keeping the same exit flow velocity, the displacement magnitude decreases for a smaller flow area. This is likely due to smaller hole size causing increased pressurization at the

free end of the tube. An increase in pressure would cause stiffening of the tube and thus reduced displacement.

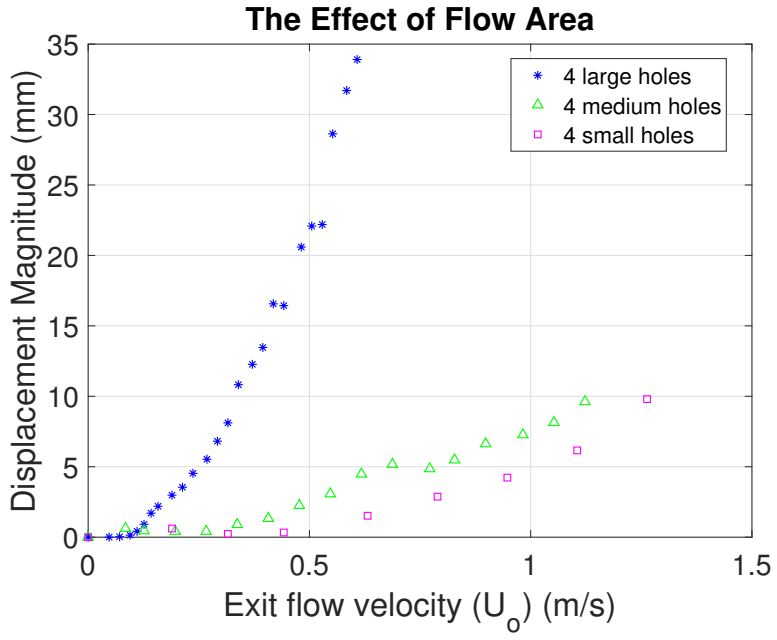

Figure 5–9: Experimental Results: Configuration (iii): Effect of Flow Area

5.2.5 The Effect of End-Piece Circumferential Symmetry

Cantilevers are highly sensitive to forces applied at the free end. Tangential forces applied to the free end cause static deflection, while axial forces may cause buckling. Since static deflection was observed experimentally, the effect of modifying the cantilever free end by adding an end-piece was observed, to see if the deflection was caused by end-piece imbalance. End-piece balance was considered here because at high enough flows for the pipe conveying fluid in water as well as air, deflection of the tube end was observed, with the magnitude of deflection substantially larger

in water. It is important to note that this deflection was considered to be static as the rms amplitude was very close to zero, showing no vibration.

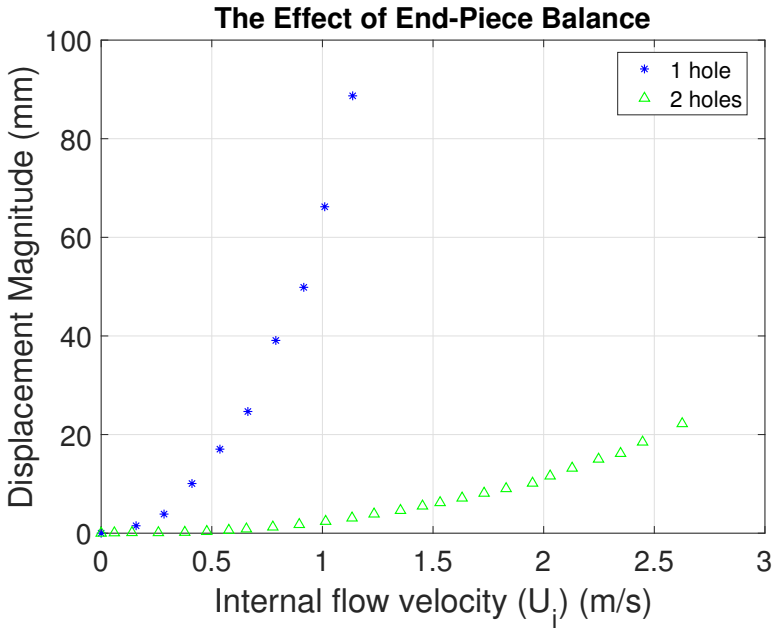

Figure 5–10: Experimental Results: Configuration (iii): Effect of End-Piece Balance

The effect of radial hole balance was tested for a radial flow end-piece with two holes. The two holes were positioned 180 degrees to one another. To unbalance the end-piece, one of the two radial holes was blocked. The results indicate a substantial increase in displacement magnitude for the unbalanced end-piece (1 hole) as compared to the balanced (2 hole) end-piece. For the same internal flow velocity, for example at 1 m/s, the 1 hole end-piece displacement magnitude was 66.2 mm while the 2 hole end-piece displacement magnitude was only 2.4 mm. This figure, Figure (5–10), demonstrates the importance of end-piece balance. For an effective radial hole end-piece, there should be uniformity in the hole size to minimize defection.

5.2.6 The Effect of End-Piece Orientation

The results presented in Figure (5–11) were for a 456 mm pipe in configuration (iii) discharging through the cantilever and aspirating through an annular space. For this set-up, the free end of the cantilever was fitted with a 4 hole end-piece, diverting the flow radially. For these 4 experiments, the end-piece was rotated by 90 degrees. In each case, static deflection was observed; however, the direction of deflection was dependent on the orientation of the end-piece. The direction of the deflection is consistent with a 90 degree rotation, as each 90 degree rotation changed the deflection by 90 degrees as well (Figure (5–11)). This implies a geometric imperfection in the end-piece.

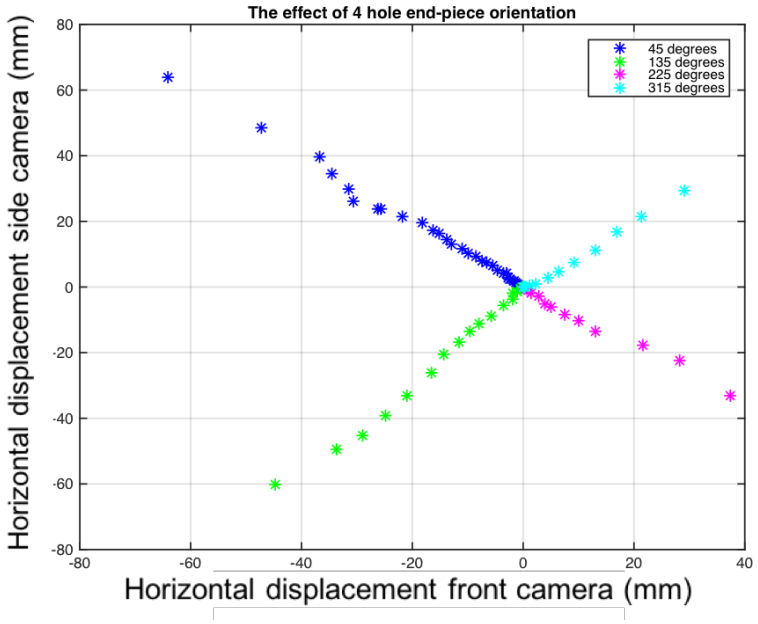

Figure 5–11: Experimental Results: Configuration (iii): Effect of End-Piece Orientation

5.2.7 Conclusions of Experimental Results for Configuration (iii)

The experimental results showed that discharging radial flow through the free end of the cantilever caused stability, while cantilevers conveying axial flow through the free end displayed loss of stability by flutter. Varying the confined length fraction r_{ann} and tube length L did not impact stability of the system, as stability was observed for all radial flow cases. However, longer tubes while stable, did display higher static displacements as compared to shorter tubes. It was also shown that the geometric tolerance of the end-piece is significant. Unbalanced end-pieces magnified the static displacement, implying that perfectly balanced end-pieces would minimize and even eliminate displacement. Additionally, geometric imperfection in the end-piece was likely since the orientation of the end-piece affected the direction of deflection. Forms of geometric imperfection could be imperfect perpendicularity between radial holes, radial hole position not exactly on the centerline of the piece, and/or slight inconsistencies in hole size.

Radial flow stability is consistent with previous experiments conducted with air flow (Rinaldi), the cantilever was also stable. In this case however, with water as the surrounding fluid, while stability was observed, static deflection also occurred. This could be the result of the buoyancy effect or added mass effect from the surrounding water causing a magnified response to geometric imperfections on the free end of the cantilever.

5.3 Comparing configuration (iii) and (iv) Radial flow

For configuration (iv) the flow is directed from the free end of the tube to the clamped end and thus entry flow is radial. Modification of the entry flow from axial

to radial did not affect the behavior or the stability of the system. However, for configuration (iii) the flow is directed from the clamped end to the free end of the tube, and thus the exit flow conditions change. Alteration of the exit flow direction from axial to radial discharge resulted in a complete change in the dynamics of the system, in which the flutter instability observed with exit axial flow was replaced by stability for radial exit flow. This observation underscores the importance of exit flow conditions as opposed to entry flow conditions.

5.4 Comparison of Experiment with Theory

The theoretical model was run for the physical experimental parameters. Results in terms of system stability or instability are reported in Table 5–1 , in which L is the cantilever tube length and L' is the outer tube length. The mass of the end-piece used was m_e=8 g, consistent with the physical component used for the experiments. The internal flow velocity (U_i) considered here ranged from 0 to 12 m/s.

Table 5–1: Experiment and Theory Comparison

L [mm]	r_{ann}	Experiment	Theory
456	0 (unconfined)	stability	stability
456	0.239	stability	stability
456	0.453	stability	instability
456	0.668	stability	stability
400	0 (unconfined)	stability	stability
300	0 (unconfined)	stability	stability
200	0 (unconfined)	stability	stability

Agreement between theory and experiment is good; in almost every case tested, stability was observed for both. Experimentally, stability was observed for every case tested. In the case of r_{ann}=0.453, however, the theoretical model predicted flutter whereas experimentally stability was observed and hence, flutter was not present. This is likely due to the model accounting for the mass of the end-piece, which theoretically has a significant effect in inducing flutter instability and even chaos in the system. Additionally, as the cantilever length was changed (L), no oscillations or flutter (stability) were observed experimentally or predicted by the theoretical model.

CHAPTER 6
Experimental Investigation
Configuration (iii) varying internal and external flow velocities

Continuation of configuration (iii) experiments was completed to explore cantilever behavior for different ratios of external flow velocity (flow through the annular space between the rigid pipe and flexible pipe) to internal flow velocity (flow through the cantilever pipe) or U_o/U_i. For these experiments, the dimensional and non-dimensional parameters are articulated in table.

6.1 Experimental Set-up

For this series of experiments, the existing apparatus was modified (Figure (6-1)). Before modifications were made to the experimental set-up, the maximum ratio of U_o/U_i was 0.0548, purely based on conservation of mass. However, to achieve greater control over the external flow velocity, a second flow meter and second centrifugal vacuum pump were subsequently integrated into the system. In this case, there are two inlets into the pressure vessel: one through the top of the pressure vessel, and one from the bottom of the pressure vessel. The flow through the top of the pressure vessel (U_i) is driven by the first pump and flows through the cantilever in the clamped-free direction. The flow through the bottom of the pressure vessel (U_{o1}) is driven by the second pump which drives flow from the bottom of the pressure vessel upward. The flow through the annular space is the external flow (U_{o2}) and is measured by the second flow meter.

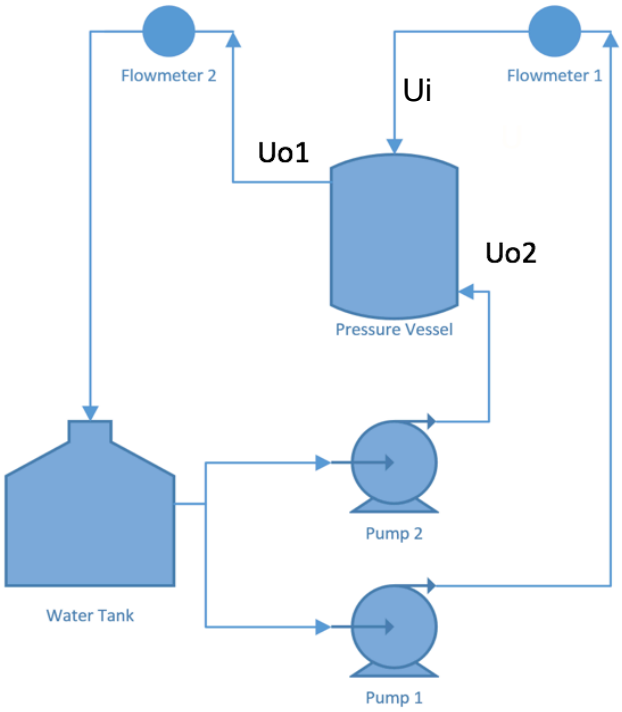

Figure 6–1: Experimental Set-Up

Again, a point very close to the free end of the tube was tracked using the Optron camera, for a 456 mm pipe fitted with a 206.5 mm outer rigid tube.

6.2 General Results

For low external flow velocity, the tube displayed first-mode flutter that grew in amplitude with increasing flow. Beyond this onset of instability, the flexible tube began to make contact with the outer rigid tube. The effect of this impacting was at first to limit motion, as the cantilever remained fixed, resting on a side of the outer tube. As flow increased, the effect of impacting resulted in the emergence

of second-mode flutter in which oscillations resumed and a higher frequency peak emerged.

6.3 Experiment type 1 Results

For this experiment, the internal flow velocity was maintained at 2 m/s while the external flow velocity was increased step-wise from 0 to 2 m/s, until a U_o/U_i ratio of 1 was reached.

Visually, the behavior of the pipe for increasing external flow velocity can be summarized as follows. Between external flow velocities 0.2 and 0.4 m/s, the flexible tube showed no visible motion. As the external flow velocity was increased to 0.45 m/s, the entire tube demonstrated low amplitude oscillations. Further increase in flow velocity resulted in maximized oscillations that were damped for periods when the flexible tube made contact with outer rigid tube. Eventually, the flexible tube rested on the outer tube and displayed low amplitude oscillatory motion that increased with increasing external flow velocity. It is significant to note that both the unconfined and confined portion of the pipe displayed oscillations that grew in amplitude with increasing flow.

6.3.1 Time Series

In Figure (6–2a), the time series is shown for an external flow velocity of 0.45 m/s, just before the cantilever tube made contact with outer tube. As seen in the figure, the displacement was sufficiently large ranging between -10 and 15 mm. For an increase in external flow velocity to 0.6 m/s, the flexible tube periodically made contact with the outer tube. As expected, this increase in external flow resulted in even larger amplitude oscillations, ranging between -10 and 25 mm. However, the

amplitude was reduced when contact was was made, as oscillations were damped (Figure (6–2b)). Although the boundary conditions change for the cantilever resting on the outer tube, several data points were recorded to characterize the behavior post-contact. This showed increase in oscillations, as seen in Figure (6–2c).

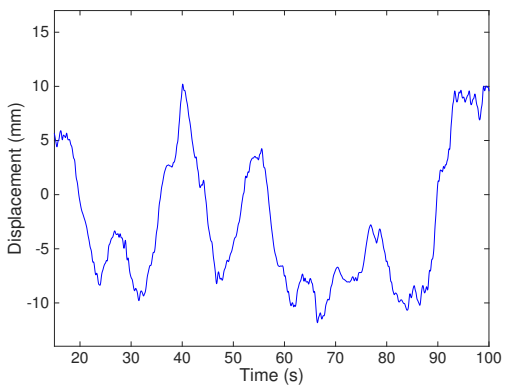

(a) U_o=0.45 m/s

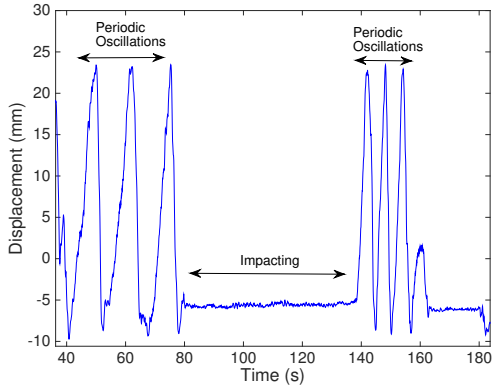

(b) U_o=0.6 m/s

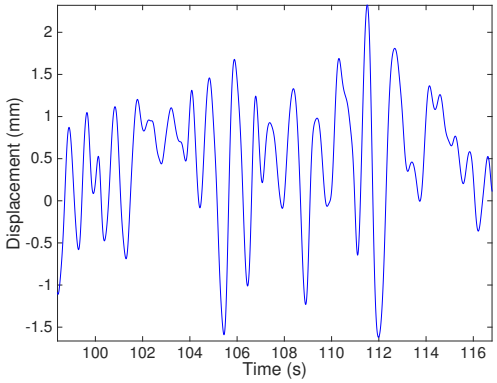

(c) U_o=1.3 m/s

Figure 6–2: Time Series for Increasing U_o

6.3.2 PSD

There is one frequency 1 Hz that starts at U_o=0.45 m/s and continues to U_o=2 m/s. This low frequency corresponds to the first-mode of vibration. A higher, second

frequency between 5 and 6 Hz, starts around an external flow velocity of 0.8 m/s. This second frequency corresponds to excitation of the second-mode, for high enough external flow velocity and after contact was made with the outer tube. As seen in the PSD (Figure (6–3)), this second frequency peak begins low in signal power but as flow velocity is increased, the peak gains signal power becoming increasingly dominant as compared to the first, lower frequency peak.

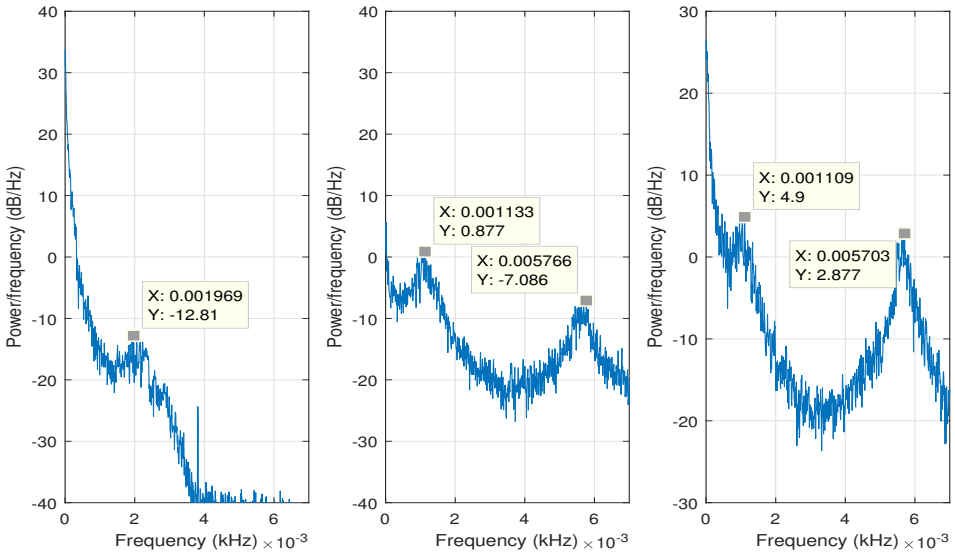

Figure 6–3: PSD: U_i=2 m/s and U_i varied

6.3.3 Rms

6.4 Experiment type 2 Results

For type 2 experiments, the internal flow velocity and external flow velocity were increased simultaneously to maintain a constant U_o/U_i ratio. Several ratios of external to internal flow velocity were considered: 0.2, 0.4, 0.6, 0.8. While several ratios were addressed here, the maximum internal and external flow velocities were

limited to stay within safe pressure levels inside the pressure vessel. Thus, the range of flow velocities tested is more limited for higher ratios.

6.4.1 0.2 Ratio

Detailed results are presented here for a U_o/U_i ratio of 0.2. Specifically for a ratio of 0.2, for U_i from 0.5 to 1.75 m/s and U_o 0.1 to 0.35 m/s, the tube showed low amplitude oscillations that were not detectable visually. Before the inner tube makes contact with the outer tube (for 0.2 ratio: U_i=0.5 to 2.5 m/s and U_o=0.1 to 0.5 m/s), oscillations are present, that reach a maximum just before impacting occurs. Figure (6–4a) shows the high amplitude oscillations that range between -10 and 25 mm. Again, for increasing flows, impacting occurs resulting in temporary suppression of motion (for 0.2 ratio: U_i=3 to 4 m/s and U_o=0.6 to 0.8 m/s). Further increase beyond the point of impacting resulted again in first and second mode flutter simultaneously. For a ratio of 0.2, this occurs in the following flow velocity ranges: U_i between 4.5 and 7 m/s and U_o between 0.9 and 1.5 m/s. It should be noted that the oscillations present after impacting becomes more chaotic and irregular as seen in Figure (6–4b). Note that trends seen here are the same as for the higher ratios.

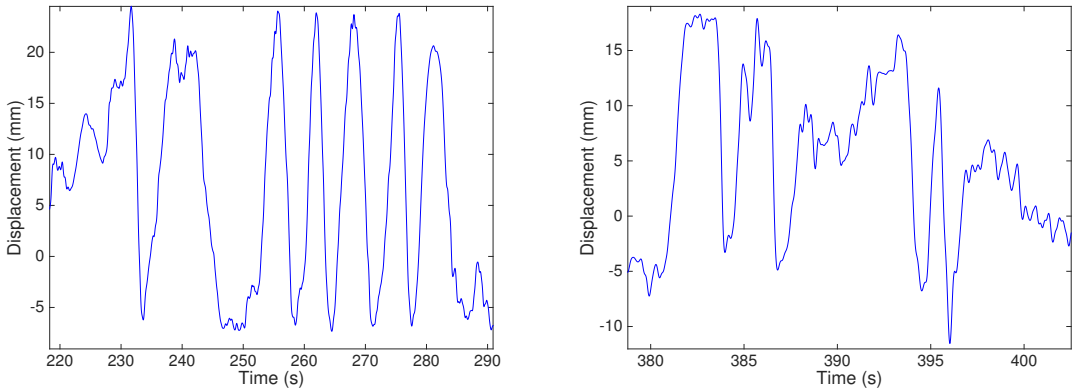

(a) U_i=2.49 m/s U_o=0.50 m/s (b) U_i=7.52 m/s U_o=1.50 m/s

Figure 6–4: Time Series for 0.2 Ratio

As seen in Figure (6–5), for lower internal and external flow, one frequency peak is present that is close to 1 Hz. For an increase in flows, two frequency peaks become evident, again referring to the first two modes of vibration.

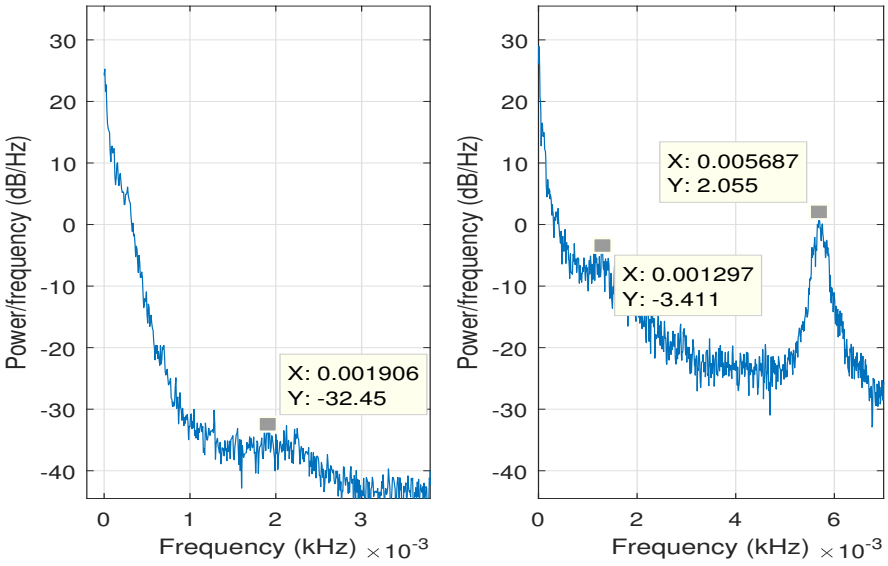

Figure 6–5: PSD: 0.2 ratio

6.4.2 Ratio Comparisons

For each ratio the internal flow velocity for which the first-mode demonstrated maximum vibration was recorded. Additionally, the U_i for which the second mode became excited was identified. These are presented as two curves in Figure (6–6) (internal flow velocity vs. U_o/U_i ratio). The first-mode showed peak vibration amplitude at 2.5 m/s of internal flow for $U_o/U_i = 0.2$. As the ratio between external and internal flow was increased, the internal flow velocity for peak vibration was reduced, indicating a de-stabilization effect for higher ratios. Additionally, the curve indicating the excitation of the second mode followed a similar trend. It can be concluded that the effect of higher ratios and higher external flow is system de-stabilization. Further verification of this claim can be seen in the rms curves in which the onset of the first-mode flutter is shown Figure (6–7). Two lines are shown in each figure; the first curve marks the pre-instability region while the second curve marks the post-instability region. The critical flow velocity associated with the onset of instability is indicated as the intersection point between these two curves. The critical flow velocity u_{cr} based on the internal flow is identified for each ratio and summarized in Table 6–1. It is evident that as the ratio increases, the critical flow velocity is decreased. This means that instability is reached for lower internal flows, again implying that higher ratios are de-stabilizing. In order to maintain stability, it is recommended to minimize external flow velocity.

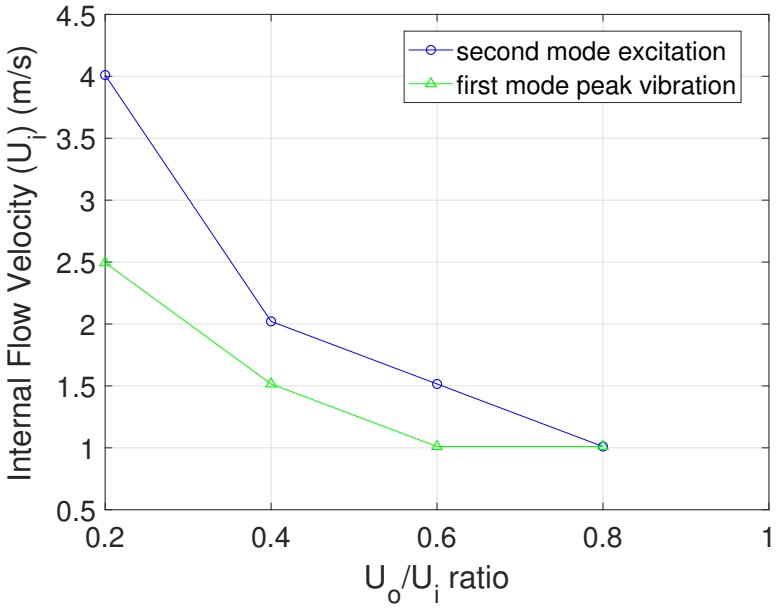

Figure 6–6: Comparing Instabilities for U_o/U_i ratios

Table 6–1: Ratio Comparisons: Experimental Critical flow velocities

Ratio	U_{cr} (m/s)
0.05	5.00
0.20	1.54
0.40	1.01
0.60	0.51
0.80	0.22

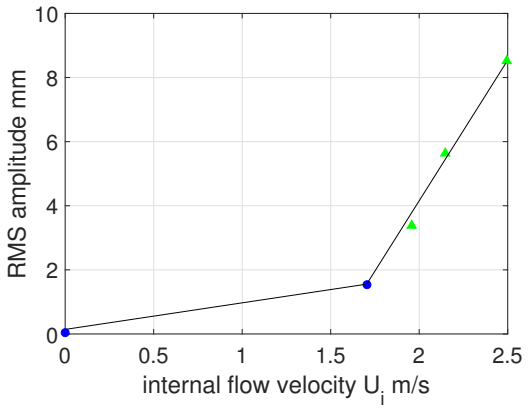

(a) 0.2

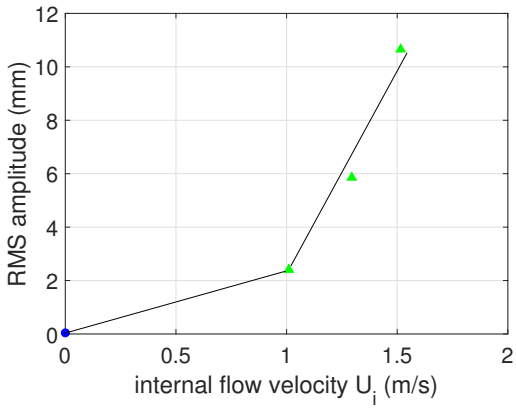

(b) 0.4

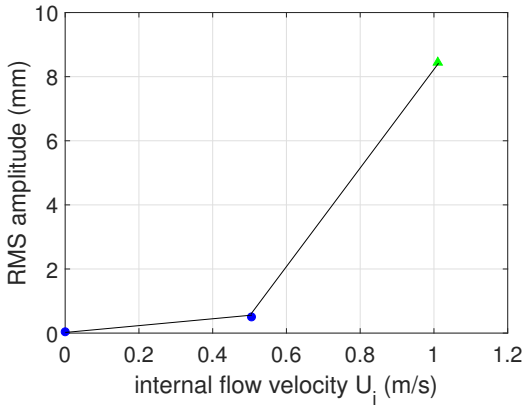

(c) 0.6

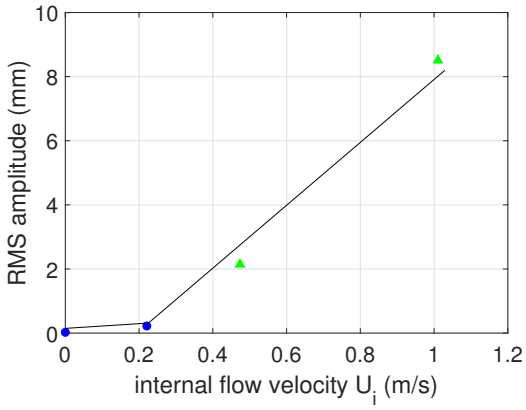

(d) 0.8

Figure 6–7: Rms for Several U_o/U_i Ratios

CHAPTER 7
Conclusion

7.1 General conclusions

Based on the experimental and theoretical investigations presented here, several general conclusions can be reached.

1. A hanging cantilever subject to configuration (iii) flow conditions with discharging flow radially from the free end exhibits stability both theoretically and experimentally. Based on the theoretical investigation of the bench-top system, stability was predicted with bench-top system parameter for several confined length fractions r_{ann}:0, 0.239, and 0.668 and for several pipe lengths: 200 mm, 300 mm, 400 mm, and 700 mm. Additionally, experimental results indicated stability for all varied parameters. Experimentally, stability was independent of cantilever length and r_{ann}. These are positive results, as elimination of flutter instability was achieved through modification of cantilever exit flow from axial to radial.
2. The theoretical model for configuration (iii) with radial exit flow conditions was tested and stability resulted for several combinations of brine-string parameters. These findings are relevant to the salt-cavern hydrocarbon storage industry as cavern geometry as wells as brine-string dimensions can be adjusted to prevent instabilities and breakage of the cantilever pipes. Modification to radial exit flow, reduction in m_e, decrease in r_{ann}, and increase in α_{ch} are

all variations in parameters that can be adjusted in the application and were proven to tend towards system stability.

3. Static deflection. Experimentally the magnitude of static deflection was independent of r_{ann}, as for all tested cases displacement magnitude remained consistent. For increasing tube length, increasing static deflection occurred. Additionally, for decreased flow area from the radial flow holes, resulted in reduced displacements. End-piece balance and orientation was also investigated and determined to be the cause of the deflection. Thus, it is important to prevent geometric imperfections near the cantilever free end.
4. Modification of exit flow has a greater impact on dynamic behavior as compared to entry flow. Altering the entry flow conditions from axial to radial flow for configuration (iv) resulted in no change in system behavior. However, altering the exit flow conditions from axial to radial flow for configuration (iii) resulted in a change in system behavior from flutter to stability.
5. Higher external flow velocity has a de-stabilizing effect on configuration (iii) systems. It was shown experimentally that higher U_o/U_i ratios resulted in lower critical flow velocities. In order to maintain stability, higher external flow velocities or annular flow should be minimized in the salt cavern application.
6. The dual camera system was necessary to capture static deflection observed for the radial flow experiments for configuration (iii). This was considered to be a significant improvement as compared to the Optron system, as with two cameras data could be recorded for two planes instead of just one.

7.2 Future Work

There are several areas in which the work presented here can be improved and expanded upon. Firstly, it would be useful to develop a theoretical model for configuration (iv) flow. As presented previously, this flow configuration is highly unstable, for both axial and radial entry flow. A theoretical model would be useful to help predict critical flow velocities as well as to adjust and experiment with parameters to see if stability can be achieved theoretically.

The radial flow investigation for configuration (iii) could be expanded in the following ways. It was previously noted that end-piece balance and geometric perfection are important for preventing static deflections observed with radial flow. Thus, improvements can be made to the existing end-piece design to ensure better balance and geometric tolerances. Additionally, different end-piece designs or methods for implementing radial flow can be researched.

Furthermore, it would be useful to adjust the existing model for configuration (iii) to account for varying U_o/U_i ratios and compare with existing experimental results.

As of now, varying U_o/U_i ratio experiments have been completed for one pipe length for one confined length fraction in configuration (iii). This investigation can be expanded to include different tube lengths and different confined length fractions. Additionally, varying U_o/U_i experiments should be completed for configuration (iv). It would be interesting to see the stabilizing or destabilizing effect of higher external flow velocities on this system.

REFERENCES

[1] T.B. Benjamin. Dynamics of a system of articulated pipes conveying fluid. *Proceedings of the Royal Society of London*, Series A261:457–486, 1961.

[2] E.F. Brater, H.W. King, J.E. Lindell, and C.Y. Wei. *Handbook of Hydraulics for the Solution of Hydraulic Engineering Problems*. McGraw-Hill, 7th edition, 1996.

[3] M.F. Butt. Experimental investigation of hanging tubular cantilevers in aspirating flow. Master's thesis, Department of Mechanical Engineering,McGill University, Montreal, Quebec, Canada, 2016.

[4] G.S. Copeland and F.C. Moon. Chaotic flow-induced vibratoins of a flexible tube with end mass. *Journal of Fluids and Structures*, 6:705–718, 1992.

[5] O. Doaré and E. de Langre. The flow-induced instability of long hanging pipes. *European Journal of Mechanics-A/Solids*, 21(5):857–867, 2002.

[6] D.B. Giacobbi. The dynamics of aspirating cantileverd pipes and pipes conveying variable density fluid. Master's thesis, Department of Mechanical Engineering, McGill University, Montreal, Quebec, Canada, 2010.

[7] R.W. Gregory and M.P. Paidoussis. Unstable oscillation of tubular cantilevers conveying fluid.i.theory. *Proceedings of the Royal Society of London. Series A. Mathematical and Physical Sciences*, 293(1435):512–527, 1966a.

[8] R.W. Gregory and M.P. Paidoussis. Unstable oscillation of tubular cantilevers conveying fluid.ii.experiments. *Proceedings of the Royal Society of London. Series A. Mathematical and Physical Sciences*, 293(1435):528–542, 1966b.

[9] M.J. Hannoyer and M.P. Paidoussis. Instabilities of tubular beams simultaneously subjected to internal and external axial flows. *ASME Journal of Mechanical Design*, 100(2):328–336, 1978.

[10] J.L. Hill and C.P. Swanson. Effects of lumped masses on the stability of fluid conveying tubes. *Journal of Applied Mechanics*, 37:494–497, 1970.

[11] N.T. Issid and M.P. Paidoussis. Dynamic stability of pipes conveying fluid. *Journal of Sound and Vibration*, 33:267–294, 1974.

[12] G.L. Kuiper and A.V. Metrikine. Dynamic stability of a submerged, free-hanging riser conveying fluid. *Journal of Sound and Vibration*, 280(3):1051–1065, 2005.

[13] G.L. Kuiper and A.V. Metrikine. Experimental investigation of dynamic stability of a cantilever pipe aspirating fluid. *Journal of Fluid and Structures*, 24(4):541–558, 2008.

[14] M.J. Lighthill. Note on the swimming of slender fish. *Journal of Fluid Mechanics*, 177(5):635–649, 1994.

[15] T.P. Luu, M.P. Paidoussis, and S. Prabhakar. Dynamics of a long tubular cantilever conveying fluid downwards, which then flows upwards around the cantilever as a confined annular flow. *Journal of Fluids and Structures*, 24(1):111–128, 2008.

[16] Y. Modarres-Sadeghi, C. Semler, M. Wadham-Gagnon, and M.P. Paidoussis. Dynamics of cantilevered pipes conveying fluid. part 3:three-dimensional dynamics in the presence of an end-mass. *Journal of Fluids and Structures*, 23:589–603, 2007.

[17] K. Moditis. The dynamics of hanging tubular cantilevers in axial flow:an experimental and theoretical investigation. Master's thesis, Department of Mechanical Engineering,McGill University, Montreal, Quebec, Canada, 2014.

[18] K. Moditis, M.P. Paidoussis, and J. Ratigan. Dynamics of a partially confined, discharging, cantilever pipe with reverse external flow. *Journal of Fluids and Structure*, 63:120–139, 2016.

[19] M.P. Paidoussis. Dynamics of tubular cantilevers conveying fluid. *IMechE Journal of Mechanical Engineering Science*, 12(2):85–103, 1970.

[20] M.P. Paidoussis. *Fluid-Structure Interactions: Slender Structures and Axial Flow, volume 1.* Academic Press, 1998.

[21] M.P. Paidoussis. Aspirating pipes do not flutter at infinitesimally small flow. *Journal of Fluid and Structures*, 13(3):419–425, 1999.

[22] M.P. Paidoussis. *Fluid-Structure Interactions: Slender Structures and Axial Flow, volume 2.* Elsevier Academic Press, 2004.

[23] M.P. Paidoussis. *Fluid-Structure Interactions: Slender Structures and Axial Flow, volume 1.* Academic Press, second edition, 2014.

[24] M.P. Paidoussis and T.P. Luu. Dynamics of a pipe aspirating fluid such as might be used in ocean mining. *ASME Journal of Energy Resources Technology*, 107(2):250–255, 1985.

[25] S. Rinaldi. Experiments on the dynamics of of cantilevered pipes subjected to internal and/or external axial flow. Master's thesis, Department of Mechanical Engineering,McGill University, Montreal, Quebec, Canada, 2009.

[26] S. Rinaldi and M.P. Paidoussis. Dynamics of a cantilevered pipe discharging fluid fitted with a stabilizing end-piece. *Journal of Fluids and Structures*, 26:517–525, 2010.

[27] C. Semler and M.P. Paidoussis. Non-linear dynamics of a fluid-conveying cantilevered pipe with a small mass attached at the free end. *Journal of Non-Linear Mechanics*, 33:15–32, 1998.

[28] V.F. Sinyavskii, V.S. Fedotovskii, and A.B. Kukhtin. Oscillation of a cylinder in a viscous liquid. *Soviet Applied Mechanics*, 16:46–50, 1980.